THESIS FOR THE DEGREE OF DOCTOR OF PHILOSOPHY

Quantum Transport Theory in Graphene

Anders Bergvall

CHALMERS

Department of Microtechnology and Nanoscience
CHALMERS UNIVERSITY OF TECHNOLOGY
Göteborg, Sweden 2014

Quantum Transport Theory in Graphene
ANDERS BERGVALL
ISBN 978-91-7597-052-3

© ANDERS BERGVALL, 2014

Doktorsavhandlingar vid Chalmers Tekniska Högskola
Ny serie nr 3733
ISSN 0346-718X

Department of Microtechnology and Nanoscience
Chalmers University of Technology
SE-41296 Göteborg
Sweden
Telephone +46 (0)31-772 1000

ISSN 1652-0769
Technical Report MC2-280

Chalmers Reproservice
Göteborg, Sweden 2014

Quantum Transport Theory in Graphene
ANDERS BERGVALL
Department of Microtechnology and Nanoscience
Chalmers University of Technology, 2014

Abstract

In this thesis, we focus on different aspects of electron transport in nanostructured graphene (such as graphene nanoribbons). We develop and implement numerical methods to study quantum coherent electron transport on an atomistic level, complemented by analytical calculations based on the Dirac approximation valid close to the points $\vec{K}$ and $\vec{K}'$ in the graphene Brillouin zone. By simulating a graphene nanogap bridged with 1,4-phenylenediamine molecules anchored via C_{60} molecules, we show that a transistor effect can be achieved by back-gating the system. By simulating STM-measurements on nanoribbons with single impurities, we investigate the interplay between size quantization and the local scatterers, and show analytically how the features of the Fourier transformed local density of states can be explained by electrons scattering between different transverse modes of the ribbons. We extend the analys to also include analytical transport calculations, and explain the origin of characteristic dips found in the transmission and their relations to quasi-bound states formed around the ribbon impurities. We construct and simulate graphene ribbons with transverse grain boundaries, and illustrate how such grain boundaries form metallic states bridging the two edges of the ribbon together. This is a plausible candidate to explain the attenuation (or even destruction) of the quantum Hall effect often seen in quantum Hall bar measurements, especially with graphene grown on metals (such as copper) where grain boundaries are common. The introductory chapters also present a basic introduction to the field of graphene and graphene ribbons, and we thoroughly present the tight-binding techniques used for simulation.

Keywords: graphene; nanoribbons; quantum coherent electron transport; tight-binding; grain boundaries; FT-LDOS

List of publications

This thesis is based on the work contained in the following papers, referred to by Roman numerals in the text:

I **Graphene nanogap for gate-tunable quantum-coherent single-molecule electronics**
A. Bergvall, K. Berland, P. Hyldgaard, S. Kubatkin, and T. Löfwander
Phys. Rev. B **84**, 155451 (2011)

II **Spectral footprints of impurity scattering in graphene nanoribbons**
A. Bergvall and T. Löfwander
Phys. Rev. B 87, 205431 (2013)

III **Basic theory of electron transport through molecular contacts**
A. Bergvall, M. Fogelström, C. Holmqvist, and T. Löfwander
To appear in "*Handbook of Single Molecule Electronics*", edited by K. Moth-Poulsen, Pan Stanford Publishers 2014

IV **Conductance footprints of impurity scattering in graphene nanoribbons**
A. Bergvall and T. Löfwander
Submitted to Phys. Rev. B

V **Destroyed quantum Hall effect in graphene with [0001] tilt grain boundaries**
A. Bergvall, J. M. Carlsson, and T. Löfwander
Submitted to Phys. Rev. Lett.

Contents

1 Introduction **1**
1.1 Thesis scope and outline 7

2 Electronic properties **9**
2.1 The graphene lattice 9
2.2 The (tight-binding) Hamiltonian and the electronic dispersion 11
2.3 Low-energy physics: the Dirac approximation 15
2.4 Pseudospin, helicity and Berry's phase 15

3 Numerical Techniques **19**
3.1 A recursive tight-binding (knitting) algorithm 21
  3.1.1 Implementation 28

4 Graphene nanoribbons **31**
4.1 Zigzag graphene nanoribbons (ZGNR's) 32
4.2 Armchair graphene nanoribbons (AGNR's) 34
4.3 Electron propagators (Green's functions) 37

5 Grain boundaries in graphene nanoribbons **41**
5.1 Grain boundaries and the coincidence site lattice model . . . 41
5.2 Quantum Hall measurements 44
5.3 Attenuation of the Quantum Hall Effect 47

6 Summary **49**

Acknowledgments **51**

A Wavefunctions and electron propagators in graphene nanoribbons **53**
A.1 Zigzag nanoribbons (ZGNR) 53

A.2 Armchair nanoribbons (AGNR) 56
A.3 Green's functions 57

B Recursive method for the computation of lead Green's functions 63

Bibliography 67

Chapter 1

Introduction

Carbon has atomic number $Z = 6$, and its uncharged atom will thus have six electrons. As illustrated in Fig. 1.1a, in the ground state, carbon has the electron configuration $1s^2 2s^2 2p^2$, which means that carbon will have two electrons in the $1s$ subshell, two electrons in the $2s$ subshell and the remaining two electrons will be in the $2p$ subshell. The first shell (consisting only of the $1s$ subshell) is full, and these (core) electrons will not be available for bonding. In the second shell (consisting of the $2s$ and $2p$ subshells), we see that there are two unpaired electrons (in the $2p$ subshell) and we would therefore expect carbon to form a maximum of two bonds if we were to hybridize two atoms in the ground state. Nature, however, likes to minimize energy, and since energy is released when a bond is formed nature would strive to maximize the number of bonds formed. Being clever enough, carbon will promote one of the electrons in the $2s$ subshell to the $2p$ subshell, as seen

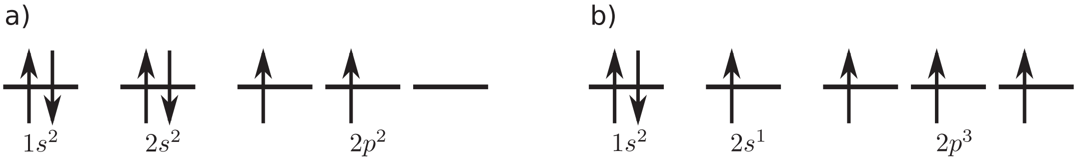

Figure 1.1: Electron configuration of carbon in a) the ground state $1s^2 2s^2 2p^2$ and b) the more bonding favourable configuration $1s^2 2s^1 2p^3$

.

in Fig. 1.1b. We now have four unpaired electrons, and after hybridizing each carbon atom can form a maximum of four bonds involving both the $2s$ and $2p$ subshells.

When hybridizing carbon atoms, we may or may not involve all of the unpaired electron orbitals in the bonding process. If all orbitals are included, one $2s$-orbital and three $2p$-orbitals will mix into what is called a sp^3-hybridization, leaving us with four sp^3-hybrid orbitals. To minimize the forces of repulsion, the hybrid orbitals will arrange themselves in space to be as far apart from each other as possible. The result is a tetrahedral structure where any bond angle will be 109.5°. All orbitals will form direct σ-bonds and the resulting structure is known as *diamond.* Since the strong orbital σ-bonds are extended in all directions in space, diamond is a very strong material that is almost impossible to break. On the other hand, since all of the four valence electrons are involved in the bonding, the electric conductivity of diamond will be zero, making diamond a very good insulator. If only two of the $2p$-orbitals are used, we will form three sp^2-hybrid orbitals instead while the remaining $2p$-orbital will be left unchanged. After minimizing repulsion, the sp^2-hybrid orbitals will all lie in the same plane with the remaining $2p$-orbital aligning perpendicular to said plane. The hybridized orbitals will form strong (in-plane) σ-bonds (with a bond angle of 120°), and the left-over $2p$-orbitals will form extended π-bonds. Due to the σ-bonds, the structure will be very strong in-plane, but since we also have an extra electron not taking part in the bonding, the structure will also be electrically conductive. A schematic picture of the different orbitals involved in the sp^2-bonding process is shown in Fig.1.2. A single layer of carbon atoms are called *graphene*, and if multiple layers are stacked on top of each other (held together weakly by van der Waals forces) we have what is known as *graphite* (where the layers easily separate, making graphite ideal as a material for standard pencils or lubricants). Serving as the building block of the different graphitic *allotropes* of carbon (see Fig. 1.3), graphene may be rolled up into *carbon nanotubes* (CNT's), or folded into *fullerene-molecules* such as the C_{60} Buckminsterfullerene (the "Bucky-ball").

Although graphite, being the most stable configuration of carbon under normal conditions, has been known to and used by man for several thousand years, the knowledge about it being made up of several one-atom thick layers is much more recent. Benjamin Collins Brodie, while studying graphite oxide, pointed out in 1859 [1] that the structure appeared to be highly

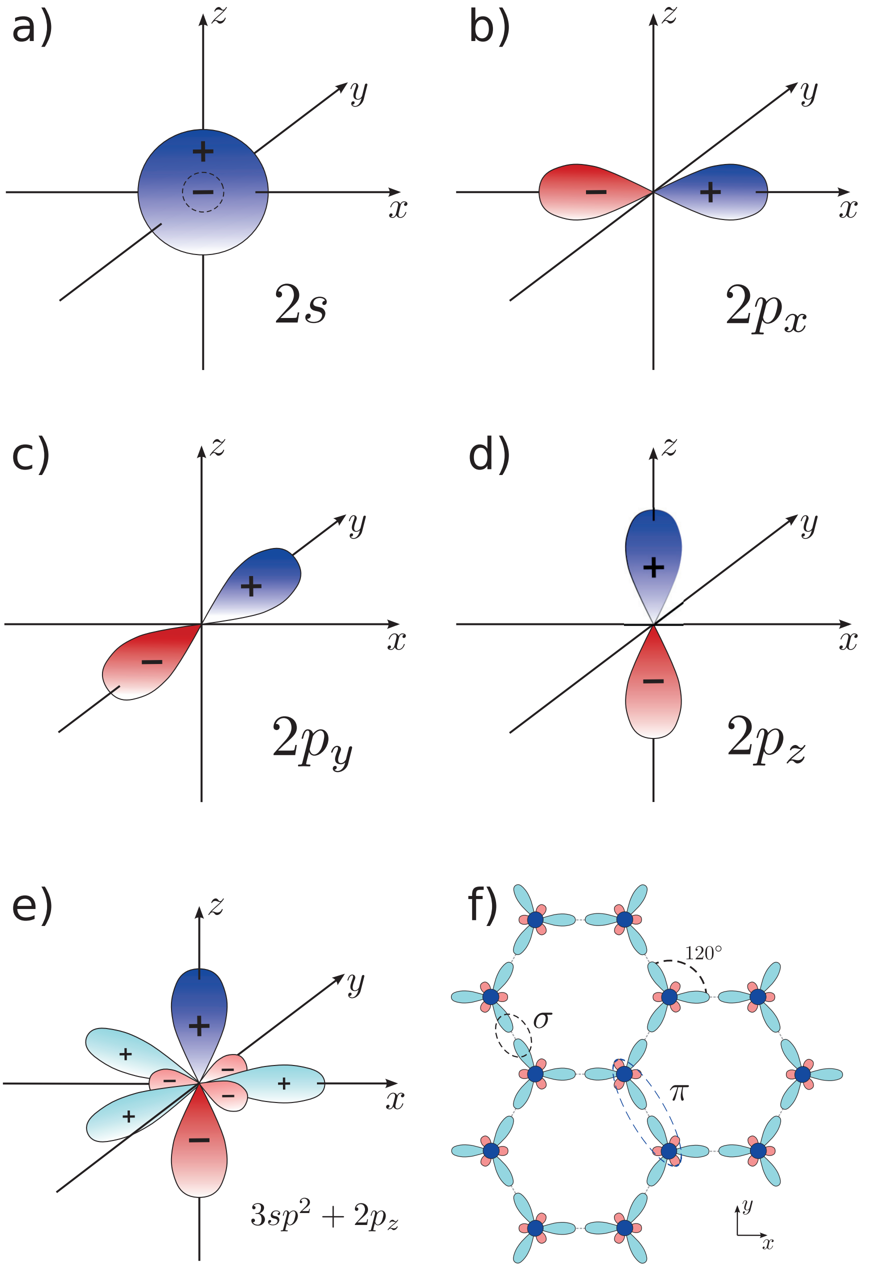

Figure 1.2: The atomic orbitals involved in the hybridization responsible for the formation of the graphene lattice: a) the spherically symmetric $2s$-orbital, b-d) the three $2p$-orbitals aligned along the x-, y- and z-axis respectively, e) the resulting hybridized $3sp^2$-orbital plus the remaining $2p_z$-orbital, and f) a topview of several orbitals forming the graphene lattice. Note how the overlap of the $3sp^2$-orbitals form σ-bonds in the graphene plane, while the $2p_z$-orbitals overlap to form π-bonds and deallocate the electrons over the graphene sheet.

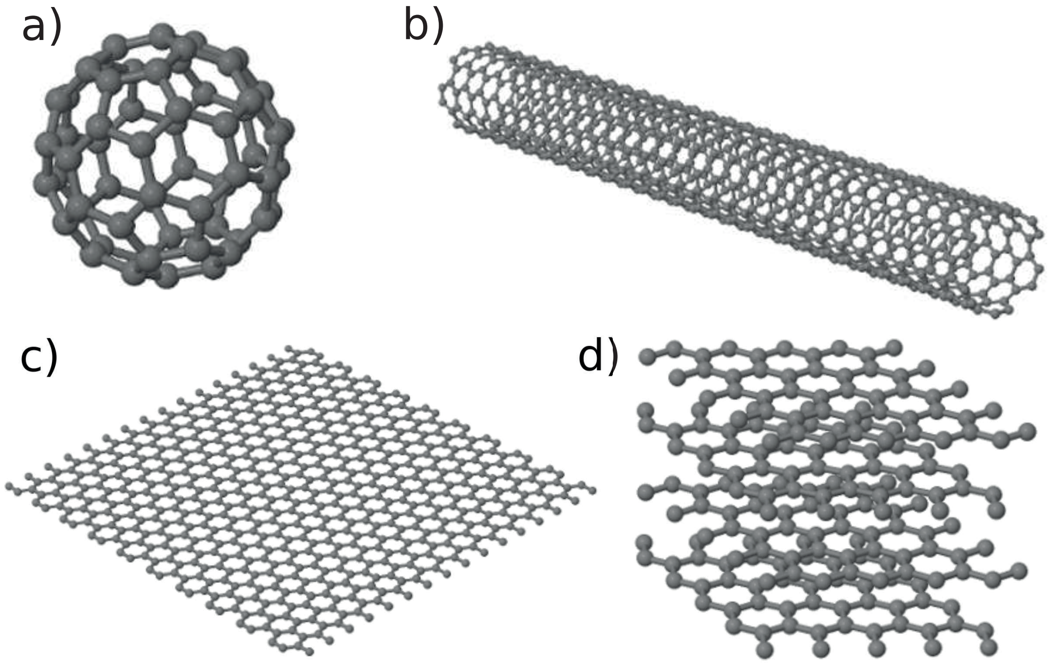

Figure 1.3: Graphitic allotropes in different dimensions: (a) 0D, C_60 fullerene (the "Bucky-ball"); (b) 1D, carbon nanotube; (c) 2D, graphene; (d) 3D, graphite.

lamellar and in half a century later, using various methods of diffraction [2, 3, 4], the crystallographic structure of graphite was resolved. Although the structure was known, single-atom layers of graphite were impossible to observe, and even more so to isolate, and not much theoretical consideration were given to them.

The first theoretical study of single-layer graphite (later named *graphene* by Boehm in 1994 [5, 6]) was done by Wallace, while working on the theoretical aspects of 3D graphite (in connection to its intended use in nuclear reactors). In his now seminal paper from 1947 [7], Wallace derived the band-structure of a "single hexagonal layer"of carbon atoms, and he noted that, close to certain points in the Brillouin zone, the dispersion of a single layer was linear with respect to momentum. The next chapter will contain a similar derivation.

Such a linear dispersion relation is usually observed if one looks at the relativistic energy-momentum relation,

$$E^2 = (pc)^2 + \left(m_o c^2\right)^2 , \tag{1.1}$$

where p is the momentum, m_0 the particles (intrinsic) rest mass, and c the speed of light. If we put the rest mass to zero, the energy-momentum relation is simplified to the linear relation $E = cp$, and it seems like electrons in graphene behave as if they were massless relativistic particles. Relativistic particles are described by the so called *Dirac hamiltonian*, after Paul M. Dirac, and the similarity between the Dirac hamiltonian and that for graphene for low energies were pointed out by Semenoff [8] and DiVincenzo and Mele [9] in 1984.

Even if a theoretical understanding of graphene was now born, it was still impossible to isolate and to observe single layers experimentally. Ruoff proposed in 1999 [10] that it should be possible to mechanically exfoliate single-layer flakes of graphene from single-crystals of graphite, but the attempts at doing so were unsuccessful and no single layers were observed. There were even doubts about whether it would be possible for graphene to exist at all [11], and the field did not evolve much under the following years. It was not until 2004, when Andrei Geim and Kostya Novoselov from the University of Manchester managed to, for the first time, both exfoliate, and isolate, single flakes of graphene that the field started to attract widespread interest again.

During one of their now famous "late friday night"-experiments (which had earlier rendered results on both Gecko-tape [12] and levitating frogs [13]...), the two scientists and their collaborators, using the method proposed by Ruoff, were able to gradually exfoliate thinner and thinner layers of graphite until only a few layers remained, using regular Scotch-tape. After placing the flakes on a silicon substrate, they were able to visually observe flakes of few-layer graphene using a simple optical microscope [14]. As pointed out by Semenoff [8], the presence of the linear type of dispersion in graphene, one should be able to observe an anomaly in the integer quantum Hall effect, if a sample of graphene was measured in a magnetic field. This was soon confirmed by Geim and Novoselov [15], and they were now sure that what they had were in fact single-layer graphene, and that the electrons were behaving like Dirac-like particles. For their discovery, Geim and Novoselov were later awarded the Nobel Price in Physics in 2010 [16, 17]. Similar studies were conducted also by Gusynin and Sharapov [18] and Zhang et al. (P. Kim's group) [19] (who published their results back-to-back with the Manchester group in Nature). The discovery of single-layer, or monolayer, graphene had created a field that were about to explode, and the amount of proposed possible practical applications of graphene would soon be impossible to keep count on. Just two weeks after the discovery in Manchester, the group of de Heer [20] managed to epitaxially grow graphene on silicon carbide (SiC), and many other techniques have been following ever since, such as (to name a few) chemical vapour deposition (CVD) growth on metal substrates, chemical synthesis or liquid phase exfoliation [21, 22, 23, 24].

As stated earlier, the possible applications for graphene are indeed numerous. In addition to being a never before seen example of a true two-dimensional material, graphene has really interesting mechanical [25] and thermal [26] properties, and has potential use and/or applications both in transistors [27], in photonics [28], in renewable energy production [29, 30, 31], and in (bio) sensing [32, 33].

The linear dispersion and relativistic nature of electrons in graphene are also predicted to behave according to the Klein-paradox (as proposed by the Swedish scientist Oskar Klein in 1929 [34]), in which the bipolar spectra of graphene allows particles to, opposite to what ones intuition might suggest, tunnel through infinitely high barriers with unity transmission (for certain angles) [35, 36]. This behaviour was verified experimentally in 2009 [37].

Other interesting and possible effects are Vaselago lensing [38] (negative refraction index) and specular Andreev reflection [39], and even the possibility of using graphene to redefine/improve the quantum resistance standard [40]. Finally, as if it was not already enough, the possibility of having bi-, tri- or multi- layered structures of stacked graphene honeycomb lattices further expands on future possibilities of graphene as a material.

The references given above are few in relation to the vaste amount of theoretical and/or experimental articles produced every day in the area of graphene. The interested reader is directed to one of the many reviews written [11, 41, 42, 43, 44, 45, 46, 47, 48, 49] and the references given therein.

1.1 Thesis scope and outline

As seen in the previous section, the field of graphene has grown really large and it is hard for everyone but a selected few to keep track of all that is going on. As a mere graduate student, my (hopeful) contribution to the giant scientific puzzle that is graphene will be focused on electron transport, and in particular how impurities in nanostructured graphene (such as ribbons) influence the electron properties. To do so, I have implemented and further developed algorithms to numerically simulate electrons on graphene lattices, and, when possible, derived analytical handles to better understand the results of the numerical simulations. Following Swedish tradition, this thesis is a *compilation thesis* where the bulk of the scientific content is found in the attached research articles. The introductory chapters are written as a help for anyone wanting to understand what is written in the articles, but they may, of course, also serve as a basic introduction to the field of graphene, quantum transport and numerical simulations. It is, however, recommended to read both the articles and the text in the introductory chapters to get all the details.

The current chapter, chapter 1, is aimed at giving a brief introduction to carbon, its most common graphitic allotropes (including graphene) and a short historical overview of how graphene was discovered together with a non-exhaustive list of its many possible applications.

In the second chapter, I will formally introduce the graphene honeycomb lattice, establish the notation I will use throughout the rest of the thesis, and try to point out some of the theoretical peculiarities that follows when trying to derive the electronic properties (such as dispersion and wave-functions) of bulk graphene.

The third chapter will present the numerical algorithms and methods used to perform tight-binding simulations on graphene lattices of arbitrary shape. Much of my time as a Ph.D student was spent on developing and implementing such methods, and I will try to give some hints and tips for anyone wanting to do the same.

In chapter 4, I will investigate what happens when bulk graphene is cut into pieces, introducing confinement. I will look at the two most common types of nanoribbons in graphene (the armchair and zigzag ribbons), derive their electronic properties, and point out their individual differences. I will introduce the electron propagators (Green's functions), and some of the results found will be compared to numerical simulations done using the techniques introduced earlier.

In the next chapter, chapter 5, I will investigate how a more complicated impurity, the grain boundary, can be constructed in graphene, and how it effects measurements involving the quantum Hall effect (studied in Paper **V**).

Finally, I will summarize the results of my work. The thesis also contains appendices, in which lengthy derivations and technical details have been placed.

Chapter 2

Electronic properties

2.1 The graphene lattice

The natural starting point, before doing anything else, is to introduce a proper definition of the honeycomb lattice (i.e., bulk graphene). Graphene has a unit cell consisting of two atoms, refered to as A- and B-atoms. After repeating the unit cell, these atoms form two triangular lattices called the A- and B-lattice, located such that each A- atom is directly neighboured by three B-atoms, as is shown in Fig. 2.1. If we by $a_0 \approx 0.142$ nm mean the separation between two neighbouring carbon atoms, the three neighbouring B-atoms to an A-atom can be reached via the neighbour vectors $\vec{c}_i$, defined as

$$\begin{aligned} \vec{c}_1 &= a_0\left(0,1\right), \\ \vec{c}_2 &= \frac{a_0}{2}\left(-\sqrt{3},-1\right), \\ \vec{c}_3 &= \frac{a_0}{2}\left(\sqrt{3},-1\right), \end{aligned} \tag{2.1}$$

and we can define two primitive lattice vectors as

$$\begin{aligned} \vec{n}_1 &= \vec{c}_2 - \vec{c}_1 = \frac{a_0}{2}\left(-\sqrt{3},-3\right), \\ \vec{n}_2 &= \vec{c}_3 - \vec{c}_1 = \frac{a_0}{2}\left(\sqrt{3},-3\right). \end{aligned} \tag{2.2}$$

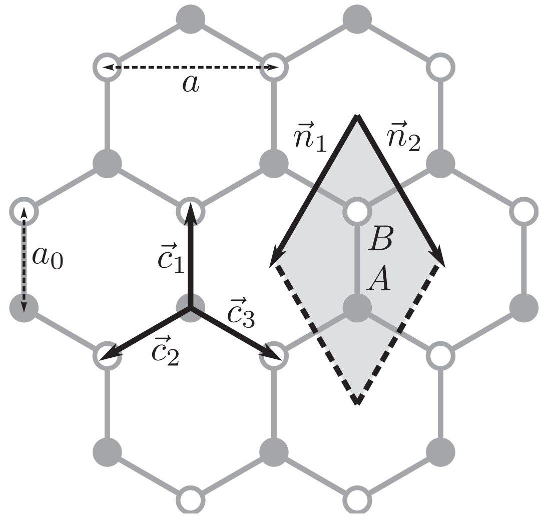

Figure 2.1: Graphene, its two triangular sublattices (the A- and B-lattice) creating the honeycomb structure, and the defining vectors.

The A-atoms are located at

$$\vec{A}_i = m_i \vec{n}_1 + n_i \vec{n}_2, \tag{2.3}$$

and the B-atoms at

$$\vec{B}_i = m_i \vec{n}_1 + n_i \vec{n}_2 + \vec{c}_1 = \vec{A}_i + \vec{c}_1, \tag{2.4}$$

where n_i and m_i are integer indices. We also introduce the lattice constant a, defined as $a = \sqrt{3}a_0$. The size of the unit cell, spanned by $\vec{n}_1$ and $\vec{n}_2$ and shown shaded in Fig. 2.1, is $\Omega_{uc} = \vec{n}_1 \times \vec{n}_2 = 3\sqrt{3}a_0^2/2 = \sqrt{3}a^2/2$.

The reciprocal primitive lattice vectors $\vec{m}_i$, found by using the definition $\vec{m}_i \cdot \vec{n}_j = 2\pi\delta_{ij}$, are

$$\begin{aligned} \vec{m}_1 &= \frac{2\pi}{3a_0}\left(\sqrt{3}, -1\right), \\ \vec{m}_2 &= \frac{2\pi}{3a_0}\left(\sqrt{3}, 1\right). \end{aligned} \tag{2.5}$$

These vectors span a hexagonal reciprocal lattice (as is shown in Fig. 2.2). The corner points of the first Brillouin zone (1BZ, shown shaded in the figure) are labeled by $\vec{K}_i$, where at $\vec{K}_1 = 4\pi/3a\,(1,0)$, $\vec{K}_2 = 2\pi/3a_0\left(1/\sqrt{3}, 1\right)$,

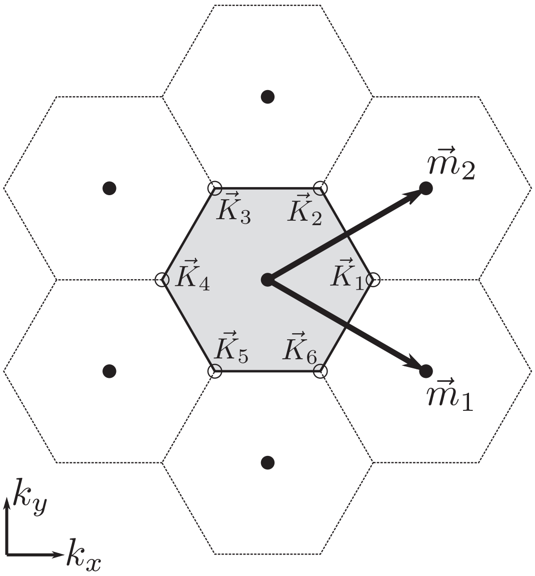

Figure 2.2: The reciprocal lattice, showing the six corner points ($\vec{K}_i$) of the first Brillouin zone (shaded hexagon) and the reciprocal lattice vectors.

$\vec{K}_3 = 2\pi/3a_0 \left(-1/\sqrt{3}, 1\right)$, $\vec{K}_4 = -\vec{K}_1$, $\vec{K}_5 = -\vec{K}_2$ and $\vec{K}_6 = -\vec{K}_3$. The area of the 1BZ is $\Omega_{1BZ} = \vec{m}_1 \times \vec{m}_2 = (2\pi/3a_0)^2 2\sqrt{3} = (2\pi)^2 2/\sqrt{3}a^2 = (2\pi)^2/\Omega_{uc}$.

2.2 The (tight-binding) Hamiltonian and the electronic dispersion

In a model of non-interacting electrons, the basic physics of graphene is captured by the tight-binding Hamiltonian

$$H = -t \sum_{<ij>} \left(a_i^\dagger b_j + b_j^\dagger a_i \right), \tag{2.6}$$

where the operators a_i and b_i annihilate (and $a_i^\dagger$ and $b_i^\dagger$ create) electrons on sites $\vec{A}_i$ and $\vec{B}_i$ respectively, t is the hopping energy and the sum is taken only over nearest neighbours i and j. To find the dispersion, we expand the annihilation operators in momentum space as

$$\begin{aligned} a_i &= \frac{1}{\sqrt{N}} \sum_{\vec{k}} e^{i\vec{k}\cdot\vec{A}_i} a_{\vec{k}}, \\ b_i &= \frac{1}{\sqrt{N}} \sum_{\vec{k}} e^{i\vec{k}\cdot\vec{B}_i} b_{\vec{k}}, \end{aligned} \tag{2.7}$$

where N is the number of unit cells in our system and $a_{\vec{k}}$ and $b_{\vec{k}}$ create electrons with momentum $\vec{k}$, which, after insertion into (2.6), gives us that

$$H = -t\frac{1}{N} \sum_i \sum_{j=1}^{3} \sum_{\vec{k}\vec{k}'} e^{i(-\vec{k}+\vec{k}')\cdot\vec{A}_i} e^{i\vec{k}'\cdot\vec{c}_j} a^\dagger_{\vec{k}} b_{\vec{k}'} + e^{i(-\vec{k}+\vec{k}')\cdot\vec{A}_i} e^{-i\vec{k}\cdot\vec{c}_j} b^\dagger_{\vec{k}} a_{\vec{k}'}. \tag{2.8}$$

Using that $\sum_{\vec{k}'} e^{i(\vec{k}'-\vec{k})\cdot\vec{A}_i} f(\vec{k}') = f(\vec{k})$, we can simplify this expression to

$$\begin{aligned} H &= -t\frac{1}{N} \sum_i \sum_{j=1}^{3} \sum_{\vec{k}} e^{i\vec{k}\cdot\vec{c}_j} a^\dagger_{\vec{k}} b_{\vec{k}} + e^{-i\vec{k}\cdot\vec{c}_j} b^\dagger_{\vec{k}} a_{\vec{k}} \\ &= -t \sum_{j=1}^{3} \sum_{\vec{k}} e^{i\vec{k}\cdot\vec{c}_j} a^\dagger_{\vec{k}} b_{\vec{k}} + e^{-i\vec{k}\cdot\vec{c}_j} b^\dagger_{\vec{k}} a_{\vec{k}}, \end{aligned} \tag{2.9}$$

or, if written on matrix form,

$$H = \sum_{\vec{k}} \begin{pmatrix} a^\dagger_{\vec{k}} & b^\dagger_{\vec{k}} \end{pmatrix} \begin{pmatrix} 0 & \phi(\vec{k}) \\ \phi^*(\vec{k}) & 0 \end{pmatrix} \begin{pmatrix} a_{\vec{k}} \\ b_{\vec{k}} \end{pmatrix}, \tag{2.10}$$

where $\phi(\vec{k}) = -t\sum_{j=1}^{3} e^{i\vec{k}\cdot\vec{c}_j}$. To simplify things even further, we rewrite the complex quantity $\phi(\vec{k})$ as an amplitude plus a phase, $\Phi(\vec{k}) = |\phi(\vec{k})|e^{i\theta_{\vec{k}}}$, where $\theta_{\vec{k}} = \arg(k_x + ik_y)$ is the angle between $\vec{k}$ and the positive k_x axis. If we also define the vector $\vec{a}^\dagger_{\vec{k}} = \begin{pmatrix} a^\dagger_{\vec{k}} & b^\dagger_{\vec{k}} \end{pmatrix}$, we have that

$$H = \sum_{\vec{k}} = \vec{a}^\dagger_{\vec{k}} h(\vec{k}) \vec{a}_{\vec{k}}, \tag{2.11}$$

where

$$h(\vec{k}) = \begin{pmatrix} 0 & \Phi(\vec{k}) \\ \Phi^*(\vec{k}) & 0 \end{pmatrix} = |\phi(\vec{k})| \begin{pmatrix} 0 & e^{i\theta_{\vec{k}}} \\ e^{-i\theta_{\vec{k}}} & 0 \end{pmatrix}. \tag{2.12}$$

The eigenvalues of the matrix $h(\vec{k})$ are given by $\pm|\Phi(\vec{k})|$, and the eigenvectors are

$$\vec{g}_{\pm}(\vec{k}) = \frac{1}{\sqrt{2}} \begin{pmatrix} 1 \\ \pm e^{-i\theta_{\vec{k}}} \end{pmatrix}. \tag{2.13}$$

This knowledge allows us to find a unitary transformation, $U(\vec{k})$, that will help us to diagonalize $h(\vec{k})$ and to find the dispersion. If we create

$$\begin{aligned} U(\vec{k}) &= \begin{pmatrix} \vec{g}_{+}(\vec{k}) & \vec{g}_{-}(\vec{k}) \end{pmatrix} = \frac{1}{\sqrt{2}} \begin{pmatrix} 1 & 1 \\ e^{-i\theta_{\vec{k}}} & -e^{-i\theta_{\vec{k}}} \end{pmatrix}, \\ D(\vec{k}) &= \begin{pmatrix} |\Phi(\vec{k})| & 0 \\ 0 & -|\Phi(\vec{k})| \end{pmatrix} = |\Phi(\vec{k})| \begin{pmatrix} 1 & 0 \\ 0 & -1 \end{pmatrix}, \end{aligned} \tag{2.14}$$

we know that we can rewrite $h(\vec{k}) = U(\vec{k})D(\vec{k})U^{\dagger}(\vec{k})$, or,

$$H = \sum_{\vec{k}} = \vec{a}^{\dagger}_{\vec{k}} U(\vec{k}) D(\vec{k}) U^{\dagger}(\vec{k}) \vec{a}_{\vec{k}}. \tag{2.15}$$

Since

$$U^{\dagger}(\vec{k})\vec{a}_{\vec{k}} = \frac{1}{\sqrt{2}} \begin{pmatrix} 1 & e^{i\theta_{vk}} \\ 1 & -e^{i\theta_{\vec{k}}} \end{pmatrix} \begin{pmatrix} a_{\vec{k}} \\ b_{\vec{k}} \end{pmatrix} = \frac{1}{\sqrt{2}} \begin{pmatrix} a_{\vec{k}} + e^{i\theta_{\vec{k}}} b_{\vec{k}} \\ a_{\vec{k}} - e^{i\theta_{\vec{k}}} b_{\vec{k}} \end{pmatrix} = \begin{pmatrix} \gamma_{+}(\vec{k}) \\ \gamma_{-}(\vec{k}) \end{pmatrix}, \tag{2.16}$$

where $\gamma_{\lambda}(\vec{k}) = \frac{1}{\sqrt{2}} \left(a_{\vec{k}} + \lambda e^{i\theta_{\vec{k}}} b_{\vec{k}} \right)$, $\lambda = \pm 1$, we arrive at the final (now diagonalized) form of the Hamiltonian

$$\begin{aligned} H &= \sum_{\vec{k}} |\Phi(\vec{k})| \begin{pmatrix} \gamma^{\dagger}_{+}(\vec{k}) & \gamma^{\dagger}_{-}(\vec{k}) \end{pmatrix} \begin{pmatrix} 1 & 0 \\ 0 & -1 \end{pmatrix} \begin{pmatrix} \gamma_{+}(\vec{k}) \\ \gamma_{-}(\vec{k}) \end{pmatrix} \\ &= \sum_{\vec{k}} |\Phi(\vec{k})| \left(\gamma^{\dagger}_{+}(\vec{k}) \gamma_{+}(\vec{k}) - \gamma^{\dagger}_{-}(\vec{k}) \gamma_{-}(\vec{k}) \right) \\ &= \sum_{\vec{k}} \sum_{\lambda = \pm 1} \epsilon_{\lambda}(\vec{k}) \gamma^{\dagger}_{\lambda}(\vec{k}) \gamma_{\lambda}(\vec{k}), \end{aligned} \tag{2.17}$$

where the bipolar dispersion is given by $\epsilon_{\lambda}(\vec{k}) = \lambda|\Phi(\vec{k})| = \lambda|\phi(\vec{k})|$, with corresponding quasi-particles (created by $\gamma^{\dagger}_{\lambda}(\vec{k})$) that are linear combinations of electronic excitations on the A- and B-lattice (with a relative phase-shift depending on the angle of $\vec{k}$ and on λ).

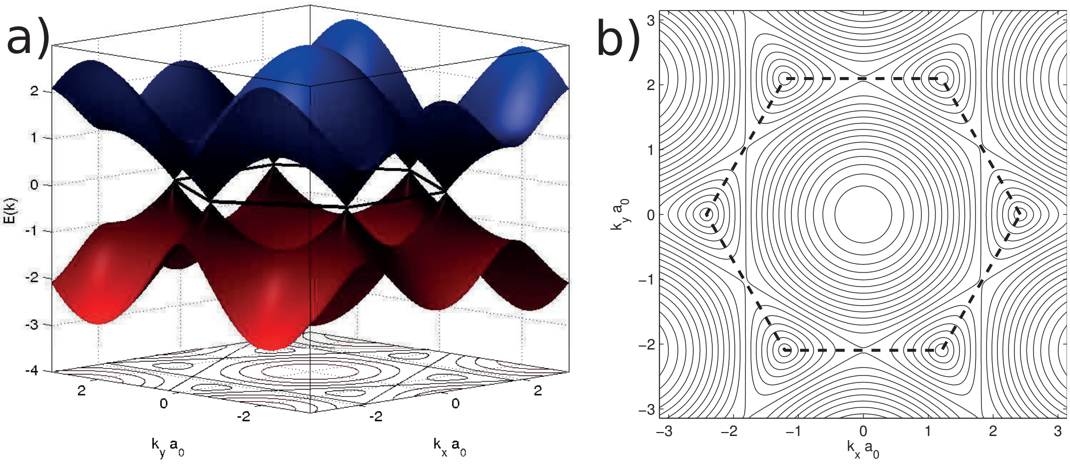

Figure 2.3: The dispersion of bulk graphene.

If we rewrite the dispersion using trigonometric functions, we find that

$$\begin{aligned}\epsilon_\lambda(\vec{k}) &= \lambda|\phi(\vec{k})| = \lambda\left|-t\sum_{j=1}^{3} e^{i\vec{k}\cdot\vec{c}_j}\right| = \dots \\ &= \lambda|t|\sqrt{1+4\cos\left(\frac{k_x a}{2}\right)\cos\left(\frac{k_y a_0}{2}\right)+4\cos^2\left(\frac{k_x a}{2}\right)}\end{aligned} \tag{2.18}$$

The dispersion (bandstructure) $\epsilon_\lambda(\vec{k})$ is plotted in Fig. 2.3a-b.

If we look at the plot of the dispersion, we see that the two bands ($\lambda = \pm 1$) touches at the points $\vec{K}_i$, where $\Phi(\vec{k})$ goes to zero. Around these points, referred to as K-points or (later) Dirac points, the constant energy contours are circular if the energy is small. For higher energies, the contours are distorted into triangular shapes (known as trigonal-warping). This is illustrated in Fig. 2.3b. We note that for any of the points in the set $\{\vec{K}_1, \vec{K}_3, \vec{K}_5\}$, we can reach the other two points in the set by a translation given by a linear combination of the reciprocal lattice vectors $\vec{m}_1$ and $\vec{m}_2$. The same is true for any of the points in the set $\{\vec{K}_2, \vec{K}_4, \vec{K}_6\}$. Thus, even though there are six K-points, only two of them (belonging to different sets) are inequivalent.

2.3 Low-energy physics: the Dirac approximation

By looking at Fig. 2.3, we learned that the two dispersion bands touch at the points $\vec{K}_i$, and we also see that the dispersion appears to be linear ($\epsilon \propto |\vec{k}|$) in the vicinity of $\vec{K}_i$. This can be shown more formally by expanding the dispersion for low energies.

Since only two of the six $\vec{K}_i$-points are inequivalent, it is enough to study one such pair of inequivalent points. We pick the two points defined by $\vec{K}^\nu = \nu\vec{K}_1 = \frac{4\pi}{3a}(\nu, 0)$, $\nu = \pm 1$, and redefine the momentum $\vec{k} = \vec{K}^\nu + \vec{\kappa}$, where $\vec{\kappa}$ is small compared to $\vec{K}^\nu$. Since $\vec{\kappa}$ is small, we can expand $\Phi(\vec{k})$ around $\vec{k} = \vec{K}^\nu$ as

$$\Phi(\vec{k}) = \Phi(\vec{K}^\nu + \vec{\kappa}) \approx \frac{3}{2}a_0 t(\nu\kappa_x - i\kappa_y). \tag{2.19}$$

If we insert this into the Hamiltonian given by (2.12), we arrive at the low-energy approximation

$$h^\nu(\vec{\kappa}) = \hbar v_f \begin{pmatrix} 0 & \nu\kappa_x - i\kappa_y \\ \nu\kappa_x + i\kappa_y & 0 \end{pmatrix} = \hbar v_f |\vec{\kappa}| \begin{pmatrix} 0 & \nu e^{-i\nu\theta_{\vec{\kappa}}} \\ \nu e^{i\nu\theta_{\vec{\kappa}}} & 0 \end{pmatrix}, \tag{2.20}$$

where $v_f = \frac{3}{2}a_0|t|/\hbar$ is the Fermi-velocity ($\approx 10^6$ m/s) and $\theta_{\vec{\kappa}} = \arg(\kappa_x + i\kappa_y)$. The low-energy eigenvalues and eigenvectors are

$$\epsilon_\lambda(\vec{k}) = \lambda|\Phi(\vec{\kappa})| = \lambda\hbar v_f|\vec{\kappa}|, \tag{2.21}$$

independent of ν, and

$$\vec{g}^\nu_\lambda(\vec{\kappa}) = \frac{1}{\sqrt{2}} \begin{pmatrix} 1 \\ \lambda\nu e^{i\nu\theta_{\vec{\kappa}}} \end{pmatrix}. \tag{2.22}$$

The dispersion for graphene in the Dirac approximation is plotted in Fig. 2.4.

2.4 Pseudospin, helicity and Berry's phase

Because of the presence of two atoms in the real space unit cell (making up the two sublattices), the wavefunctions of graphene are two-component vectors (or pseudospinors). Using the Pauli matrices,

$$\sigma_x = \begin{pmatrix} 0 & 1 \\ 1 & 0 \end{pmatrix}, \quad \sigma_y = \begin{pmatrix} 0 & -i \\ i & 0 \end{pmatrix}, \quad \sigma_z = \begin{pmatrix} 1 & 0 \\ 0 & -1 \end{pmatrix}, \tag{2.23}$$

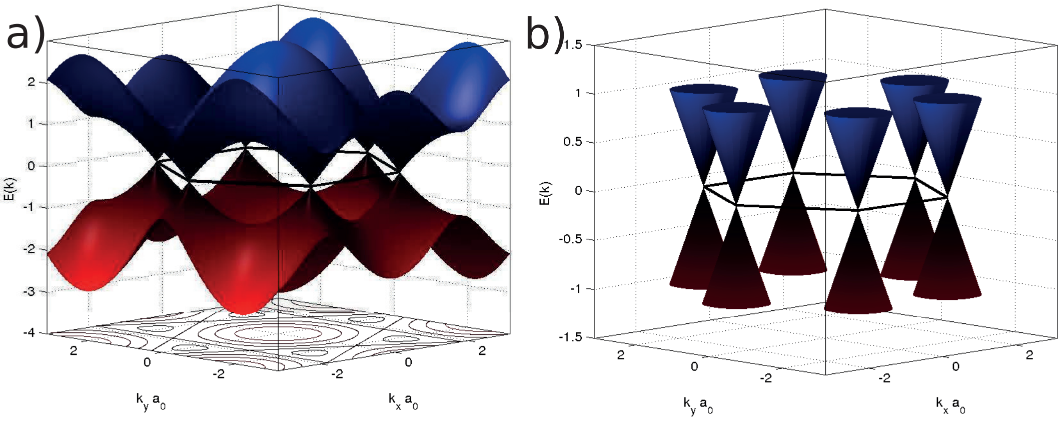

Figure 2.4: The Dirac approximation, valid in the vicinity of the K-points

the low-energy Hamiltonian can be rewritten as

$$h^{\nu}(\vec{\kappa}) = \hbar v_f \left(\nu \kappa_x \sigma_x + \kappa_y \sigma_y \right) \tag{2.24}$$

or

$$h(\vec{\kappa}) = \begin{cases} \hbar v_f \vec{\sigma} \cdot \vec{\kappa} & \text{around } \vec{K}^{+}, \\ -\hbar v_f \vec{\sigma}^{*} \cdot \vec{\kappa} & \text{around } \vec{K}^{-}, \end{cases} \tag{2.25}$$

where $\vec{\sigma} = (\sigma_x, \sigma_y)$ and $\vec{\sigma}^{*} = (\sigma_x, -\sigma_y)$.

When dealing with normal electron spin, one often talks about the projection of the spin onto a fixed axis (such as the z-axis, given by the operator σ_z). Another concept, that of *helicity*, is defined as the projection not on a fixed axis, but on the direction of momentum (i.e., the direction the particle is moving). If the spin (or pseudospin, in the case of graphene) points in the same direction as the momentum, the helicity is said to be *right-handed*, or *positive*. If the opposite is true, that the pseudospin points in the opposite direction of the momentum, the helicity is *left-handed* or *negative*. The helicity-operator is given (in our low-energy notation) by

$$\tilde{h} = \frac{1}{2} \frac{\vec{\sigma} \cdot \vec{p}}{|\vec{p}|} = \frac{1}{2} \frac{1}{|\vec{\kappa}|} \begin{pmatrix} 0 & \kappa_x - i\kappa_y \\ \kappa_x + i\kappa_y & 0 \end{pmatrix}, \tag{2.26}$$

and we directly see that around the point $\vec{K}^{+}$ (since the helicity operator is then directly proportional to $h(\vec{\kappa})$), we have that

$$\tilde{h} \vec{g}^{+}(\vec{\kappa}) = \frac{1}{2|\vec{\kappa}|} \frac{1}{\sqrt{2}} \begin{pmatrix} \lambda(\kappa_x - i\kappa_y) e^{i\theta_{\vec{\kappa}}} \\ \kappa_x + i\kappa_y \end{pmatrix} = \lambda \frac{1}{2} \vec{g}^{+}(\vec{\kappa}). \tag{2.27}$$

Thus, around $\vec{K}^+$, the helicity is positive for positive energies (in the conduction band), and negative for negative energies (in the valence band). At the other K-point, $\vec{K}^-$, graphene litterature often (confusingly) states that the same relation holds [50] but with an opposite sign, i.e. that $\tilde{h}\vec{g}^-(\vec{\kappa}) = -\lambda\vec{g}^-(\vec{\kappa})$. This is, as seen by inspection, not totally true in the notation we use, and the confusion arises because people often do not clearly state what coordinate systems they use, and in what basis their calculations are done. If we would change $\kappa_x \to -\kappa_x$ around the point $\vec{K}^-$, the relation would hold. In other words, for the relation to hold it requires that we use a left-handed local coordinate system around $\vec{K}^-$. We may, just as well, just redefine the helicity-operator in that area to be left-handed (by using the left-handed Pauli matrices, $\tilde{h}^- = \frac{1}{2}\frac{\vec{\sigma}^*\cdot\vec{\kappa}}{|\vec{\kappa}|}$, where $\vec{\sigma}^* = (\sigma_x, -\sigma_y)$, instead). Then,

$$\tilde{h}^-\vec{g}^-(\vec{\kappa}) = -\lambda\frac{1}{2}\vec{g}^-(\vec{\kappa}), \tag{2.28}$$

and we see that the eigenvalues now comes with an opposite sign. This can also be seen directly by looking at (2.25), where we see that a helicity operator proportional to $\vec{\sigma}\cdot\vec{p}$ will not be a conserved quantitiy around $\vec{K}^-$ (it does not commute with $H \propto -\vec{\sigma}^*\cdot\vec{\kappa}$, while a helicity operator proportional to $-\vec{\sigma}^*\cdot\vec{p}$ does). Thus, the helicity around the point $\vec{K}^-$ is the opposite to that of $\vec{K}^+$. The concept of helicity in graphene is illustrated in Fig. 2.5.

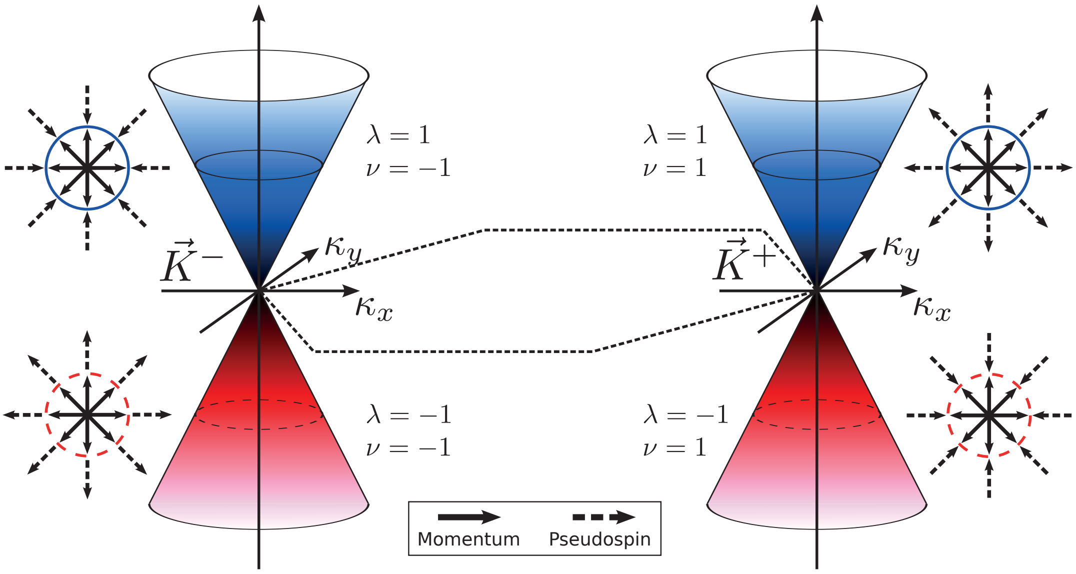

Figure 2.5: Helicity in graphene.

The Berry-phase is defined as (C is a closed contour around one of the

Dirac-points)

$$\begin{aligned}\theta_B &= -i \oint_C d\vec{\kappa}\ [\vec{g}^{\nu}_{\lambda}(\vec{\kappa})]^{\dagger}\ \frac{\partial}{\partial \vec{\kappa}}\ \vec{g}^{\nu}_{\lambda}(\vec{\kappa}) \\ &= -i\frac{1}{2}\int_0^{2\pi} d\theta_{\vec{\kappa}}\ \begin{pmatrix} 1 & \lambda\nu e^{-i\nu\theta_{\vec{\kappa}}} \end{pmatrix} \frac{\partial}{\partial \theta_{\vec{\kappa}}} \begin{pmatrix} 1 \\ \lambda\nu e^{i\nu\theta_{\vec{\kappa}}} \end{pmatrix} \\ &= \frac{1}{2}\nu \int_0^{2\pi} d\theta_{\vec{\kappa}} = \nu\pi, \end{aligned} \tag{2.29}$$

which is different from the normal case where going around a close loop would introduce a phase shift that is a multiple of 2π (i.e., no phase-shift at all). For graphene, the pseudospinors are such that a phase-shift of $\pm\pi$ is achieved [51] and the wavefunction changes sign. This phenonemenon was observed earlier in research on carbon nanotubes [52, 53].

Chapter 3

Numerical Techniques

In (very) simplified terms, the basic constituents of the systems we will simulate are 1) a (often large) number N of atoms (or sites) located in real space on the positions $\vec{r}_i$, where $i \in [1, N]$, 2) a given overlap of the different orbitals belonging to the different atoms, and 3) electrons that can move around ("hop") between the atoms. The electrons may, or may not, interact with each other, directly or indirectly.

A non-interacting (free) electron currently located at atomic site j have two choices. It may either remain (associated with the *onsite energy* ϵ_i), or it may hop to any other atomic site i where the orbital overlap is non-zero (associated with a *hopping energy* t_{ij}). As simple as it sounds, this model, known as a *tight-binding* model, can then be used to extract several interesting properties of the system. The parameters ϵ_i and t_{ij} are (often) found through complicated overlap integrals between the different atomic orbitals, or they can be extracted from experiment or found in literature.

If we introduce the operators a_i and $a_i^\dagger$ that annihilates (creates) an electron on site j, the processes described above may be written as the Hamiltonian

$$H = \sum_i \epsilon_i a_i^\dagger a_i + \sum_{i \neq j} \left(t_{ij} a_i^\dagger a_j + h.c. \right). \tag{3.1}$$

This is the same type of Hamiltonian as the one shown in (2.6), although

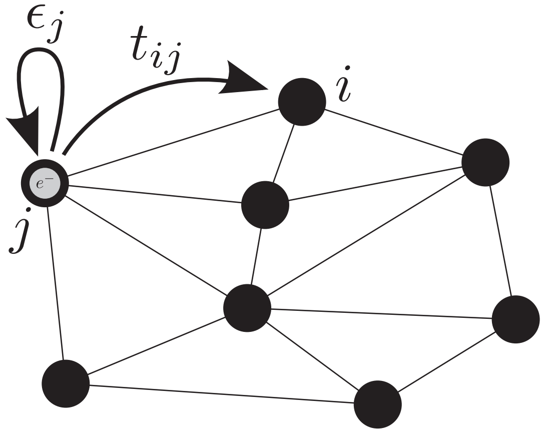

Figure 3.1: A schematic sketch of a tight-binding process in which an electron can either remain on atomic site j (energy ϵ_j), or hop to another site j (energy t_{ij}).

we have now dropped the division into an A- and B-lattice.

If we want to draw the atomic system, we usually mark the atomic positions with filled circles, and if the hopping element between two atoms is non-finite, the circles are connected with a line. A sketch of such a system is shown in Fig. 3.1.

The Hamiltonian in (3.1) may also be written on matrix form. This Hamiltonian matrix will be of size $N \times N$, where the elements will correspond to $H_{ii} = \epsilon_i$ and $H_{ij} = t_{ij}$. By inverting this Hamiltonian, we may find the systems (retarded) Green's function matrix, defined as

$$G_{ij}(E) = (E + i\eta - H)^{-1}, \tag{3.2}$$

from which we can then extract properties such as, e.q., the local density of states [given by $\rho_i(E) = -(1/\pi)\mathrm{Im}G_{ii}(E)$].

The problem with calculating the Green's function as given in (3.2) is that matrix inversion is a very costly operation. By brute force, inverting a $N \times N$ matrix will require $\mathcal{O}(N^3)$ operations, and as the system size N grows large, direct inversion becomes intractable. There are, however, numerous tricks one can use, based on the facts that 1) the matrix H is usually very sparse, and 2) one normally do not require the knowledge of all the elements of $G_{ij}(E)$. The matrix is sparse since the orbital overlap will vanish between atoms that are located far from each other, and one usually considers finite t_{ij}'s only when atoms i and j are nearest, or next-nearest, neighbours.

One trick is to divide the system into smaller parts (often slices), perform matrix inversion on the smaller slice Hamiltonians, and then link the slice Green's functions together using recursion. These methods, usually known as *slice-by-slice* methods, are well established [54, 55, 56, 57, 58]. If a system of N atoms can be divided into N' subsystems each containing M atoms, the computational complexity can be reduced since inverting $N' = N/M$ matrices of size $M \times M$ requires only $\mathcal{O}(NM^2)$ operations, which (for $M << N$ offers a significant speed-up). A more elaborate discussion about such methods are given in Paper **III**.

Even if they are conceptually simple, the slice-by-slice methods are usually restricted to systems with very specific geometries (often linear, such as ribbons where it is easy to repeat the same slice over and over again, although recent development also allows non-linear, multi-terminal structures [59]). Here, we will look at another algorithm which allows complete flexibility in terms of the system geometry, internal degrees of freedom and number of attached leads/contacts, while preserving the improved computational performance of the slice-by-slice methods.

3.1 A recursive tight-binding (knitting) algorithm

The algorithm we will use was first proposed by Kazymyrenko and Waintal [60] (see also [61]), and is more or less the above partitioning of the system into smaller sub-systems (slices) taken to the extreme. Namely, what happens if the slices consists of only a single atom, turning matrix inversion into the problem of normal scalar division?

We start with the same system as earlier, consisting of N atoms located at positions $\vec{r}_i$, $i \in [1, N]$. Here, we will add the possibility of each atom having internal degrees of freedom. This allows us to also include the effects of, e.g., electron spin (up/down) or electron/holes. Depending on the situation, the parameters ϵ_i and t_{ij} are either scalars or matrices of size $D \times D$ where D is the number of internal degrees of freedom for each atom. By reducing the slice-size to one, we will find our Green's functions by building the system one atom at a time.

We define the Green's function G^A_{ij} as the propagator from site j to i in a system where the first A atoms has already been included (or "knitted"). The Green's function of the first atom, G^1_{11}, is trivial, and is given by $G^1_{11} = g^1_{11}$, where

$$g^1_{11} = \left[E + i\eta - \epsilon_1\right]^{-1}. \tag{3.3}$$

At this point, we have calculated everything there is to know about the system so far. The next step is to add the second ($A = 2$) atom. The difference is now that the system now already contains atom 1, and we do not start with empty space. Instead, we must take into account the effects of atom 1 already being added, which is done by using the Dyson equation.

First, we calculate the (unperturbed) Green's function of atom 2 before connecting it to the system as

$$g^2_{22} = \left[E + i\eta - \epsilon_2\right]^{-1}. \tag{3.4}$$

Once this is known, we use the Dyson equation to find that

$$G^2_{22} = g^2_{22} + g^2_{22} t_{21} G^2_{12}, \tag{3.5}$$

$$G^2_{12} = g^1_{11} t_{12} G^2_{22}, \tag{3.6}$$

so that

$$G^2_{22} = g^2_{22} + g^2_{22} t_{21} g^1_{11} t_{12} G^2_{22}. \tag{3.7}$$

After rewriting this expression, we find that

$$G^2_{22} = \left[1 - g^2_{22} t_{21} g^1_{11} t_{12}\right]^{-1} g^2_{22}, \tag{3.8}$$

or, after noting that $g^1_{11} = G^1_{11}$,

$$G^2_{22} = \left[1 - g^2_{22} t_{21} G^1_{11} t_{12}\right]^{-1} g^2_{22}. \tag{3.9}$$

Since there is now a connection between atoms 1 and 2, we can also calculate the Green's function between these atoms:

$$G^2_{12} = G^1_{11} t_{12} G^2_{22} \tag{3.10}$$

and

$$G^2_{21} = G^2_{22} t_{21} G^1_{11}. \tag{3.11}$$

Finally, we have that

$$\begin{aligned}
G_{11}^{2} &= G_{11}^{1} + G_{11}^{1} t_{12} G_{21}^{2} \\
&= G_{11}^{1} + G_{11}^{1} t_{12} G_{22}^{2} t_{21} G_{11}^{1} \\
&= G_{11}^{1} + \underbrace{G_{11}^{1} t_{12} G_{22}^{2}}_{=G_{12}^{2}} \left[G_{22}^{2}\right]^{-1} \underbrace{G_{22}^{2} t_{21} G_{11}^{1}}_{=G_{21}^{2}} \\
&= G_{11}^{1} + G_{12}^{1} \left[G_{22}^{2}\right]^{-1} G_{21}^{1}.
\end{aligned} \tag{3.12}$$

After calculating these Green's functions, we once again know everything about the system after having added atoms 1 and 2. In the same way, we go on adding new atoms one by one, until we arrive at having added the last atom, where $A = N$.

Next, we realize that if we want to calculate the propagator G_{AA}^{A}, all we need to know is the propagators between all atoms in the set σ that are neighbours of atom A (that is, all atoms where $t_{\sigma A}$ and $t_{A\sigma}$ are finite, and where the atoms have already been connected, i.e., where $\sigma < A$). An atom can be either partially connected (some of its neighbours are still to be added to the system), or fully connected (an atom where all of its neighbours are already added). We define the set of all partially connected atoms as a (or b).

The general expression for G_{AA}^{A} can be written

$$\begin{aligned}
G_{AA}^{A} &= \left[E + i\eta - \epsilon_A - g_{AA}^{A} \sum_{\sigma\sigma'} t_{A\sigma} G_{\sigma\sigma'}^{A-1} t_{\sigma' A}\right]^{-1} g_{AA}^{A} \\
&= \left[\left[g_{AA}^{A}\right]^{-1} - g_{AA}^{A} \sum_{\sigma\sigma'} t_{A\sigma} G_{\sigma\sigma'}^{A-1} t_{\sigma' A}\right]^{-1} g_{AA}^{A}.
\end{aligned} \tag{3.13}$$

The propagator to any already added atom α in the system from atom A (or from any already added atom β to A) is given if know the propagators to any of the atoms σ neighbouring atom A , plus the propagator G_{AA}^{A}, since

$$G_{\alpha A}^{A} = \sum_{\sigma} G_{\alpha\sigma}^{A-1} t_{\sigma A} G_{AA}^{A} \tag{3.14}$$

and

$$G_{A\beta}^{A} = \sum_{\sigma} G_{AA}^{A} t_{A\sigma} G_{\sigma\beta}^{A-1}. \tag{3.15}$$

Finally, the propagators between atoms α and β are given by

$$G^{A}_{\alpha\beta} = G^{A-1}_{\alpha\beta} + G^{A}_{\alpha A}\left[G^{A}_{AA}\right]^{-1} G^{A}_{A\beta}. \tag{3.16}$$

In the above, we have assumed that all N atoms are included in the set α (or β), but we will soon see that we do not need to include more than a couple of them. First, however, we look at what happens if our system is also connected to one or several leads.

An example system is shown in Fig. 3.2, where the central system is connected to three leads. We assume that the Green's functions for the contact atoms (the atoms in the leads, shown with white circles, that has neighbours in the system) are known (for an example algorithm showing how to calculate these, see Appendix. B). Instead of starting from the first black atom, we assume that our system already contains the contact atoms. The contact atoms are included in the set c (or d). We will need to constantly update any propagators going from/to a contact atom, so the set c will from now on always be a subset of α. Instead of letting all already connected atoms (there is A of them at each step) being part of α, only the contact atoms plus the atoms currently being partially connected (the set a) are included.

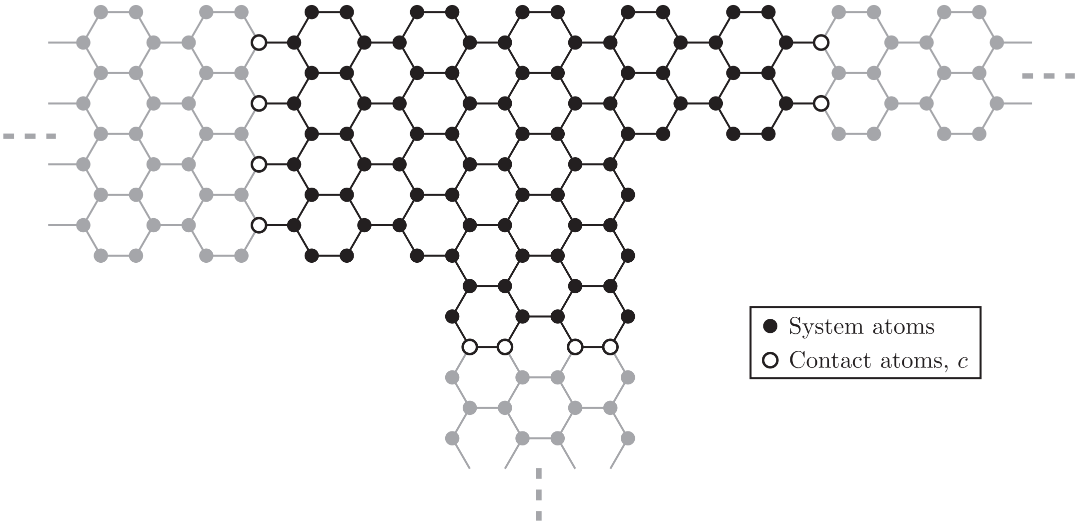

Figure 3.2: Example system with three attached semi-infinite leads (gray atoms). The lead atoms (contact atoms) connected to the system are illustrated with white circles, and the system atoms with black circles.

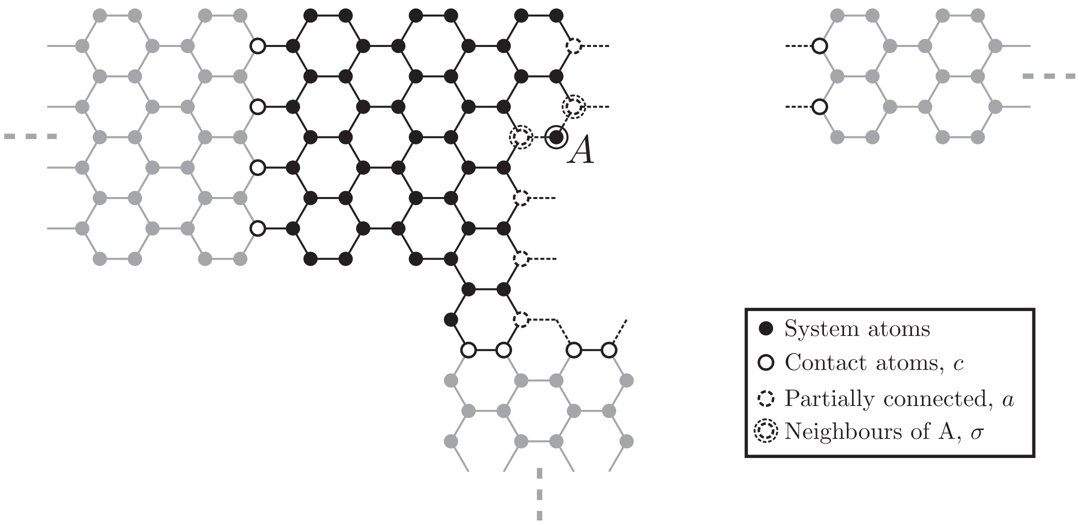

Figure 3.3: The system when adding atom A. The interface (α) consists of the contact atoms (c, full white circles) and the system atoms still missing one or more neighbours (a, dashed white circles). The atom A has two neighbours (σ, dashed double-circles) that are already connected. Note that σ is always a subset of a.

To make things clearer, consider Fig. 3.3, where we enter the calculation approximately when half of the system atoms have been added. The different sets of atoms (a, c and σ) are marked in the figure, and our set α consists of, as stated earlier, the contact atoms (c) plus the partially connected atoms (a). We can then go on and calculate G^A_{AA}, $G^A_{\alpha A}$, $G^A_{A\beta}$ and finally $G^A_{\alpha\beta}$. When this is done, A is connected to the system and, if necessary (such as if it still has neighbours to be connected), added to the sets a and/or σ. At the same time, all atoms in a that are now fully connected are removed from this set.

After all of the N atoms are connected, the first part of the algorithm (referred to as the "knitting"-part by Kazymyrenko and Waintal) is completed. Since all contact atoms were kept in α, we now have the propagators between all of the contact atoms, and we may easily calculate transmission between any two of the leads. For example, in our example system, if c_1 are the contact atoms in the left lead (a subset of c), and c_2 the contact atoms of the right lead (another subset of c), we find the transmission from lead

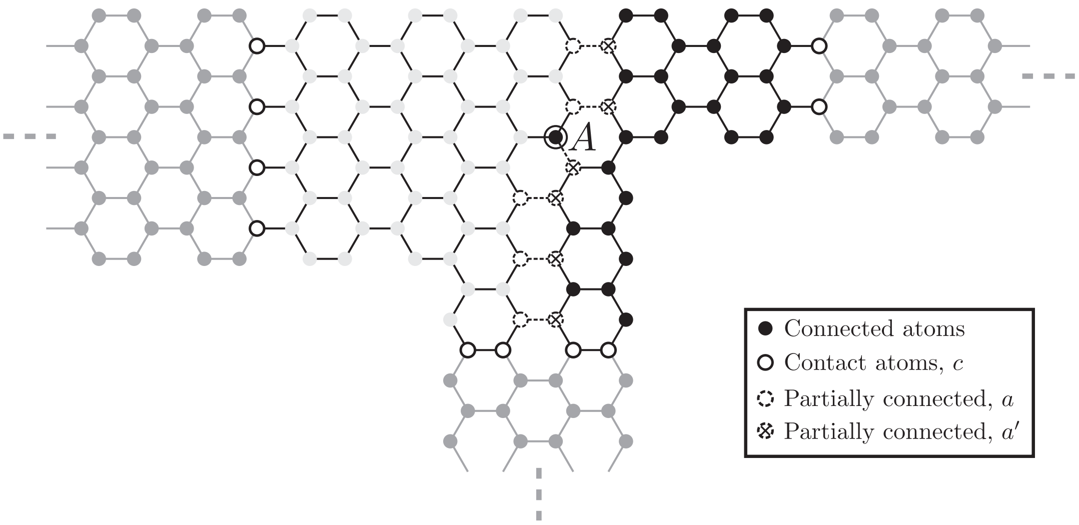

Figure 3.4: The system while going backwards to calculate local properties (”sewing”). We now have two sets of partially connected atoms, a and a', that needs to be updated for each step A.

c_1 to c_2, G_{21}, from the formula

$$T_{21} = \sum_{\gamma,\gamma'\in c_1} \sum_{\delta,\delta'\in c_2} \Gamma_{\gamma\gamma'} G_{\gamma'\delta} \Gamma_{\delta\delta'} \left(G_{\gamma\delta'}\right)^*, \tag{3.17}$$

where the contact self energies, Γ, are calculated as in Appendix B.

The next part of the algorithm, called the ”sewing”-part, will allow us to also calculate local properties such as bond currents. For this, we need the complete Green’s functions between all neighbours in the system, and not only those between contact atoms. This is achieved by going backwards again, starting from atom $A = N$ and arriving at atom $A = 1$. In Fig. 3.4, we have once again reached atom A (same atom as in Fig. 3.3). The set a is the same at it were after A was knitted into the system, and we have also introduced another set called a' (or b'), which contains all atoms that are partially connected when moving backwards. The complete Green’s functions between any atom in the set a' and A may be found from the relations

$$G_{a'A} = \sum_{ab'} G_{a'b'} t_{b'a} G^A_{aA}, \tag{3.18}$$

$$G_{Ab'} = \sum_{ba'} G^A_{Ab} t_{ba'} G_{a'b'}, \tag{3.19}$$

and we also have that

$$G_{AA} = G^A_{AA} + \sum_{ba'} G^A_{Ab} t_{ba'} G_{a'A}. \tag{3.20}$$

Here, we see that we need the functions G^A_{aA} and G^A_{Ab}. These functions needs to be stored for each step during the knitting-part of the algorithm, which is no problem since the sets a (and b) where exactly the same then. Once A has been sewn, it is added to the set a', and the algorithm continues until we arrive back at atom $A = 1$. Meanwhile, since we get the complete Green's functions between A and its neighbours in the primed set a', we can easily calculate local properties such as bond currents or local density of states. The local density of states is given by

$$\rho_A = -\frac{1}{\pi}\mathrm{Im}G_{AA}, \tag{3.21}$$

and the bond-current between A and a neighbour σ' in a' is given by

$$I_{\sigma' A} = \frac{e}{h}\int dE\ G^<_{\sigma' A} t_{A\sigma'} - G^<_{A\sigma'} t_{A\sigma'}. \tag{3.22}$$

Here, the lesser Green's functions, $G^<$, is given by

$$G_{\sigma' A} = \sum_l f_l(E) \sum_{c_l d_l} G_{\sigma' c_l} \Gamma_{c_l d_l} \left(G_{A d_l}\right)^* \tag{3.23}$$

and

$$G_{A\sigma'} = \sum_l f_l(E) \sum_{c_l d_l} G_{A c_l} \Gamma_{c_l d_l} \left(G_{\sigma' d_l}\right)^*, \tag{3.24}$$

where c_l and $f_l(E)$ are the contact atoms belonging to, and the Fermi-function of, contact l respectively.

Performance-wise, the bottleneck of the knitting-part is equation 3.16, which requires a total of N vector-vector multiplications, scaling as $\mathcal{O}(NM^2)$. Here, M is the size of the interface α, and if the atoms are ordered in such a way that M on average is much less than N, we have the same performance as the slice-by-slice method, as stated earlier. The same applies to the sewing-step, where the scaling of the bottlenecks [equations (3.18)-(3.20)] scale as $\mathcal{O}(LNM^2)$, where L is the number of neighbours to each atom ($L \leq 3$ in the case of graphene with nearest-neighbour hopping only).

Memory-wise, the big restriction is that we need to save a lot of data to be able to perform the sewing-step. For each knitting-step, the vectors G^A_{aA} and

G^A_{Ab} needs to be stored, which requires $\mathcal{O}(NM)$ in memory consumption. Using double floating point precision, a single complex number requires 128 bits which generates a total memory requirement on the order of $128 \times NM$. Thus, 2 Gigabytes of RAM will be enough to store 62.5×10^6 elements, which would be enough for a square rectangular grid of 400×400 atoms. If we were to attach contacts on both sides of this square lattice, the size of M would be three times larger, and the maximum grid size would be greatly reduced to only 130×130 atoms, while the computational cost would be nine times larger. Thus, practical restrictions on both memory and time limits the maximum system size to a couple of hundred thousand atoms. As mentioned in [60], there are ways to also recursively calculate the vectors G^{A-1} from G^A [by reshuffling (3.16)], reducing the memory consumption to $\max(N, M^2)$. This additional step is, however, a bit tedious to implement and for the system sizes we are considering we are fine without modifiying the algorithm.

In the following chapters, I will use the numerical algorithm to perform tight-binding simulations. The simulations will serve both as "numerical labwork", and as complements to our analytical results.

3.1.1 Implementation

To implement the knitting algorithm, I recommend using a fast programming language such as C/C++ or Fortran. To handle the matrix and vector operations required, great speed-up is achieved by using optimized packages such as BLAS. In my work, I used Intel Fortran and Intel MKL [62], which is highly optimized for the Intel CPU architecture, and also easily parallelizable through the use of OpenMP [63, 64].

The system geometry is stored in linked lists, which allow for easy insertion/removal of atoms, and the possibility to link blocks of atoms together. Each atom contains a link to all of its neighbour atoms. The system setup (such as atomic positions, onsite energies, hopping energies, which atoms are neighbours, etc.) are stored in input files read by the Fortran program. To generate these input files, a scripting language such as Python is highly recommended. To define what atoms are neighbours, the easiest way is to use their coordinates and define a distance cutoff, r_c, such that all atoms lying closer than r_c together are considered neighbours. This can be done using a k-d tree [65].

Since the working matrices (that are only stored once, and updated regularly), like $G^{A}_{\alpha\beta}$ and $G_{a'b'}$, only contain a fraction of the N atoms at the same time, we can not adress an atom by using its index number A. This because the size of the working matrices are only $\alpha \times \alpha$. This problem is solved by giving each atom a new index (a knit-index, between 1 and the size of α), and to make sure that two atoms appearing (at any time) in the same set (α) do not have the same knit-index. My solution is to use an "index-bank". When an atom is being added to the system (the contact atoms are added first), it borrows an index from the index-bank. When the atom has been fully connected, it will no longer appear in a set, and its index can then be returned to the index-bank to be lended out to a new atom instead. If the index-bank is constructed in a last in, first out (LIFO) way, this will make sure that the number of required knit-indices are kept to a minimum, and that no index-conflict arises.

Chapter 4

Graphene nanoribbons

Graphene nanoribbons are created by cutting a sheet of graphene into the shape of a ribbon. When doing so, the edges of the ribbon will have different properties depending on in which direction the ribbon is cut out. As we have defined our graphene lattice (recall Fig. 2.1 and see Fig. 4.1), cutting along the x-axis would produces ribbons with *zigzag* edges, where as cutting along the y-direction (or a direction rotated 30 degrees from the x-axis) would generate what is called *armchair* edges. These are the two most common edges available, and we will now see how the electronic properties and band structure [66, 67, 68, 69] of the generated ribbons differ from each other depending on the edges in question.

In the low-energy approximation, the wavefunction of any ribbon can be taken as a combination of momenta around the two different K-points (or Dirac points) $\vec{K}^{\nu}$, where $\nu = \pm 1$:

$$\vec{\Psi}(\vec{r}) = e^{i\vec{K}^{+}\cdot\vec{r}}\vec{\psi}^{+}(\vec{r}) + e^{i\vec{K}^{-}\cdot\vec{r}}\vec{\psi}^{-}(\vec{r}), \tag{4.1}$$

where $\vec{K}^{\nu} = K(\nu, 0)$, $K = 4\pi/3a$, and where

$$\vec{\psi}^{\nu}(\vec{r}) = \begin{pmatrix} \psi^{\nu}_{A}(\vec{r}) \\ \psi^{\nu}_{B}(\vec{r}) \end{pmatrix} \tag{4.2}$$

are the pseudospinors containing the contributions from the two sublattices A and B. To find the wavefunctions, and the corresponding disper-

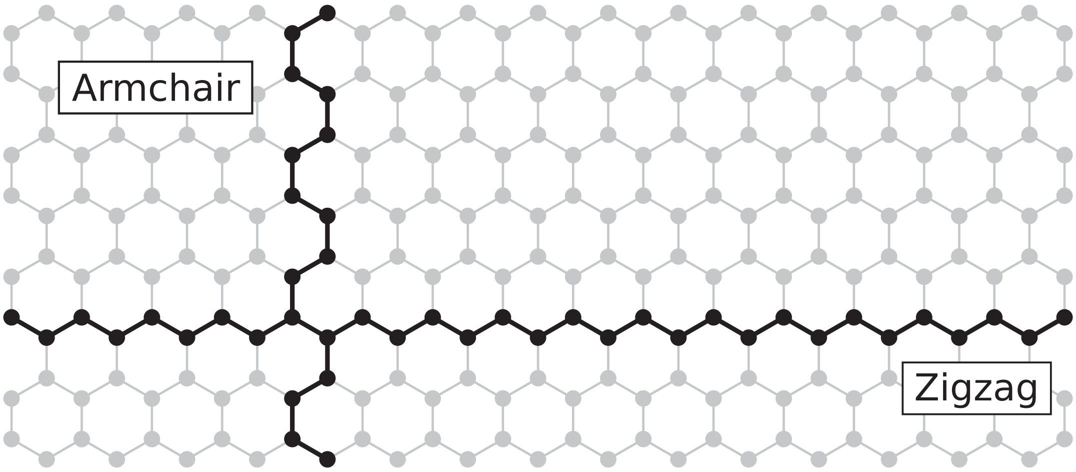

Figure 4.1: The two most common edges in graphene nanoribbons: Zigzag and Armchair.

sion/bandstructure, we must solve the eigenvalue problem

$$h^{\nu}(\vec{\kappa})\vec{\Psi}^{\nu}(\vec{r}) = \epsilon(\vec{\kappa})\vec{\Psi}^{\nu}(\vec{r}). \tag{4.3}$$

Depending on what type of ribbon edge we select, we will have to impose different boundary conditions and quantization of $\vec{\kappa}$.

4.1 Zigzag graphene nanoribbons (ZGNR's)

A typical Zigzag graphene nanoribbon (ZGNR) is shown in Fig. 4.2. If we by N mean the number of horisontal carbon chains (the ribbon in the figure has $N = 6$), we see that the ribbon unit cell (the shaded rectangle in the figure) will contain a total of $M = 2N$ atoms. The distance between the edge atoms (shown as crosses), or the width of the ribbon, is

$$W = (3N + 2)\frac{a_0}{2}. \tag{4.4}$$

By looking at the figure, we see that on one of the edges, all atoms belong to the same sublattice. The proper boundary condition for the ZGNR is thus that

$$\Psi_A(x, y = 0) = \Psi_B(x, y = W) = 0. \tag{4.5}$$

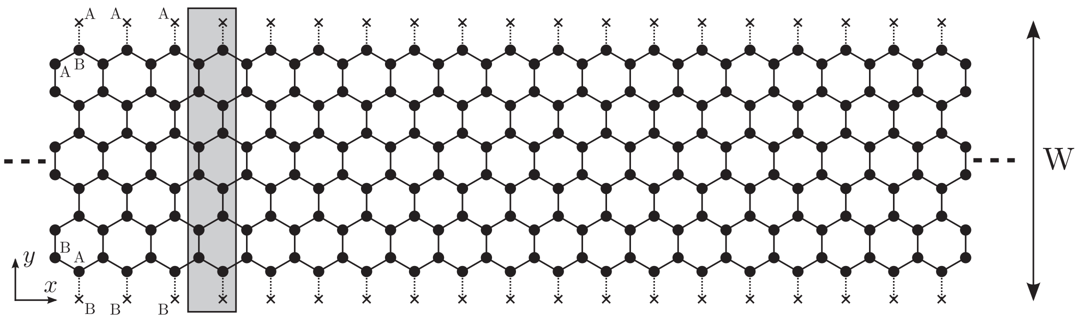

Figure 4.2: A zigzag graphene nanoribbon (ZGNR) with $N = 6$. The unit cell (the shaded box) contains $2N$ atoms. To make the wavefunction vanish on the edges (marked with crosses), the A-lattice (B-lattice) component of the wavefunction must be zero at $y = W$ $(xy0)$.

After putting this into (4.3) we find that (for a complete derivation, see Appendix A.1) that the transverse momenta, κ_n, and the longitudinal momenta, κ_x, are coupled and given by

$$\nu\kappa_x = -\frac{\kappa_n}{\tan(\kappa_n W)}. \tag{4.6}$$

If κ_n is allowed to become imaginary, $\kappa_n = iq_n$, we also have solutions where

$$\nu\kappa_x = -\frac{q_n}{\tanh(q_n W)}. \tag{4.7}$$

Neither one of these equations are analytically solvabled, but we may use numerics to find the dispersion, $\epsilon_{\lambda n}(\kappa_x) = \lambda\hbar v_f\sqrt{\kappa_x^2 + \kappa_n^2}$. The dispersion for the ZGNR with $N = 51$, calculated using tight-binding, is shown in Fig. 4.3a. The analytical solutions for low energies, around $\nu = 1, \lambda = 1$ are shown in Fig. 4.3b, and we see that the overlap of the numerical and analytical solutions are quite good for low energies.

The wavefunction pseudo-spinor are given by (see Appendix. A.1)

$$\Psi_A(\vec{r}) = 4iC_A^{\nu}e^{i\kappa_x x}\cos(Kx)\sin(\kappa_n y) \tag{4.8}$$

and

$$\Psi_B(\vec{r}) = 2i\lambda C_A^{\nu}e^{i\kappa_x x}\left[e^{-iKx}\sin(\kappa_n y + \theta_+(\vec{\kappa})) + e^{iKx}\sin(\kappa_n + \theta_-(\vec{\kappa}))\right], \tag{4.9}$$

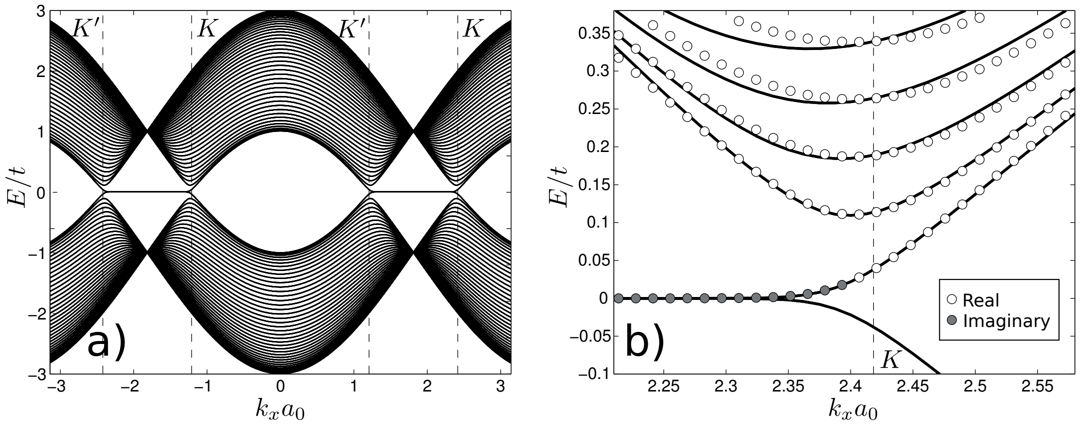

Figure 4.3: The dispersion of a Zigzag ribbon (N = 51), calculated using a) tight binding and b) the Dirac approximation in the vicinity of the right K-point ($\nu = 1, \lambda = 1$). The real solutions are plotted as white dots, and the imaginary solutions are plotted as gray dots.

where $\theta_\nu(\vec{\kappa}) = \arg(\nu\kappa_x + i\kappa_n)$ and the normalization constant is given by

$$C_A^\nu = \frac{1}{2}\sqrt{\frac{\kappa_n}{2\kappa_n W - \sin(2\kappa_n W)}}. \tag{4.10}$$

The transversal part of the wavefunction components are plotted in Fig. 4.4 for a couple of different states on the lowest energy sub-band. We see that each component vanishes on one side, and that when the solutions of κ_n becomes imaginary the wavefunctions localizes on the other edge.

4.2 Armchair graphene nanoribbons (AGNR's)

A ribbon created by cutting along the armchair direction is shown in Fig. 4.5. In the figure, the coordinate axes has been flipped to make for an easier fit. If the number of full carbon rings inside the ribbon unit cell (shaded rectangle) is defined as N (the ribbon in the figure has $N = 5$), the unit cell will contain $M = 4N + 2$ atoms, and the width of the ribbon will be

$$W = (N + 1)\sqrt{3}a_0 = (N + 1)a. \tag{4.11}$$

By inspection, we see that the boundary condition is now that the wavefunctions on both sublattices vanish on both edges (since each edge has both

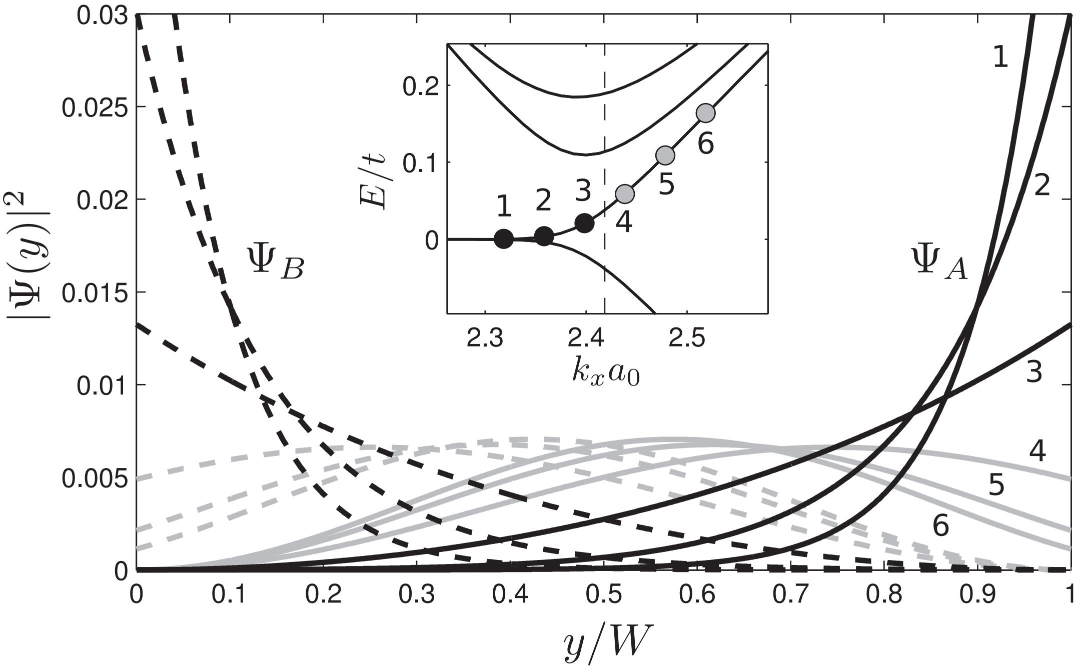

Figure 4.4: Wavefunctions of a ZGNR ($N = 41$) in the lowest subband, for different values of k_x around K. Note how the imaginary solutions (shown in black) localizes at one of the edges.

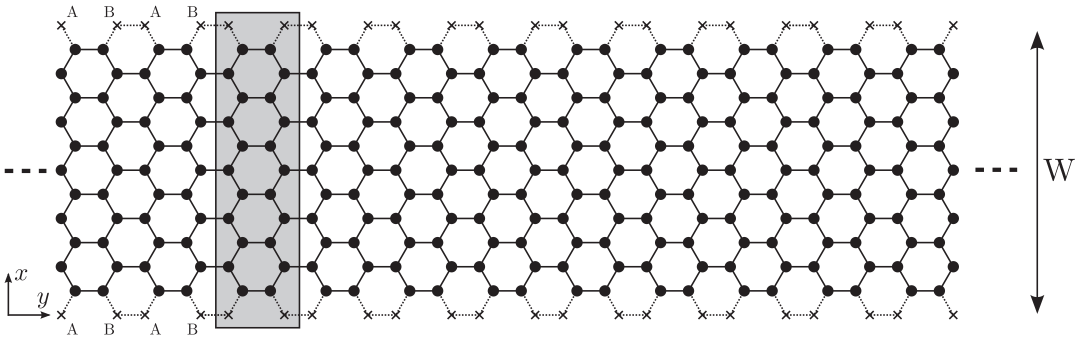

Figure 4.5: An armchair graphene nanoribbon (AGNR) with $N = 5$. The unit cell (the shaded box) contains $4N + 2$ atoms. To make the wavefunction vanish on the edges (marked with crosses), both the A- and B-lattice components must be zero on both edges (at $x = 0$ and $x = W$).

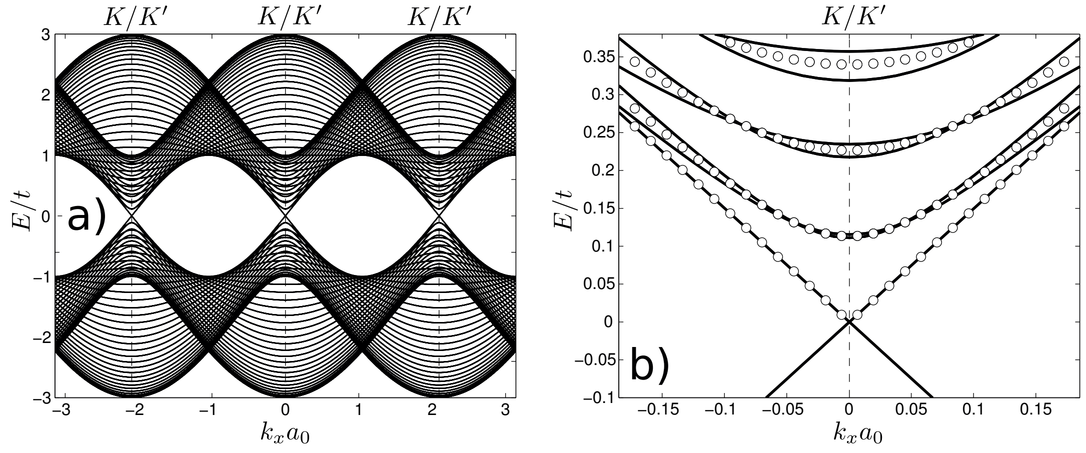

Figure 4.6: The dispersion of an Armchair ribbon (N = 23, metallic), calculated using a) tight binding and b) the Dirac approximation ($\lambda = 1$).

A- and B-atoms), i.e.,

$$\vec{\Psi}(x = 0, y) = \vec{\Psi}(x = W, y) = 0. \tag{4.12}$$

As shown in Appendix A.2, insertion into and solving (4.3) gives us that

$$\kappa_n = \frac{n\pi}{W} - K = \frac{n\pi}{W} - \frac{4\pi}{3a}, \tag{4.13}$$

and the longitudinal momentum κ_y is not coupled to the transverse momenta κ_n (as were not the case for the zigzag ribbons). The dispersion, given by $\epsilon_{\lambda n}(\kappa_y) = \lambda\hbar v_f\sqrt{\kappa_n^2 + \kappa_y^2}$, will have a gap at $\kappa_y = 0$ as long as $\kappa_n \neq 0$, and the AGNR will be semiconducting. For certain values of N, we will, on the other hand, have that $\kappa_n = 0$ and the ribbon will be metallic. The condition for this to occur is that we can find an integer solution n to the equation

$$n = \frac{4(N + 1)}{3}. \tag{4.14}$$

This is only possible if $N + 1$ is a multiple of 3, i.e., when $N = 3m - 1$. Thus, depending on the width, the armchair ribbon may be either metallic or semiconducting. The dispersions for the AGNR's with $N = 23$ (metallic), $N = 24$ (semiconducting) are shown (together with full numerical tight-binding calculations) in Fig. 4.6 and Fig. 4.7.

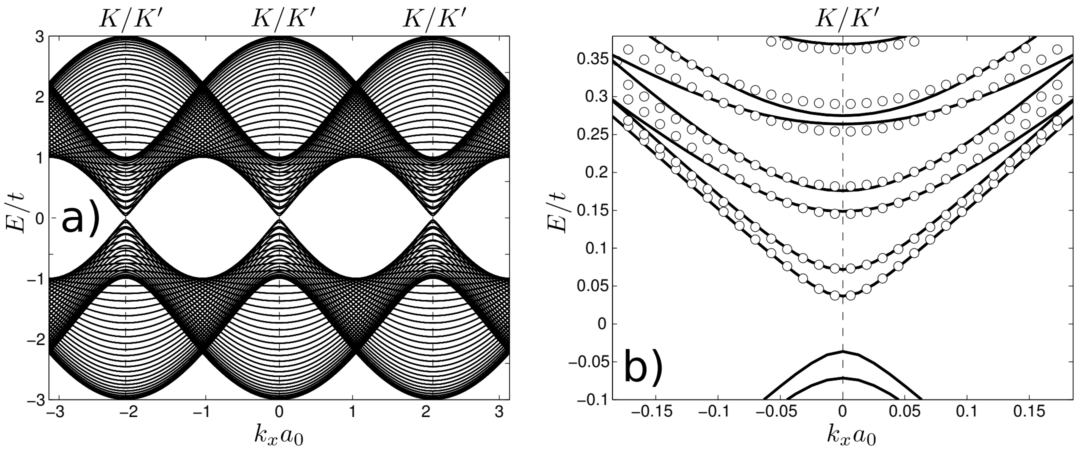

Figure 4.7: The dispersion of an Armchair ribbon (N = 24, semiconducting), calculated using a) tight binding and b) the Dirac approximation ($\lambda = 1$).

The wavefunction pseudo-spinor is given by (see Appendix. A.2)

$$\vec{\Psi}_n(\vec{r}) = \begin{pmatrix} i \\ \lambda e^{i\theta(\vec{\kappa})} \end{pmatrix} \chi_n(x) e^{i\kappa_y y}, \tag{4.15}$$

where $\theta(\vec{\kappa}) = \arg(\kappa_y - i\kappa_n)$ the transverse wavefunctions are $\chi_n(x) = \sqrt{1/W}\sin(\frac{n\pi}{W}x)$. These functions are zero on both edges, and the armchair ribbon does not have the edge states found for the zigzag ribbon.

4.3 Electron propagators (Green's functions)

Once the wavefunctions are known, the retarded electron propagator (or retarded Green's function), between the points $\vec{r}\,'$ to $\vec{r}$ (in the transverse mode n), for a ribbon may be calculated by using the Lehmann representation

$$g_n(\vec{r}, \vec{r}\,'; E) = \sum_{\lambda=\pm 1} \int_{-\infty}^{\infty} \frac{d\kappa_y}{2\pi} \frac{\vec{\Psi}_n(\vec{r})\vec{\Psi}_n^{\dagger}(\vec{r}\,')}{E + i\eta - \epsilon_{\lambda n}(\kappa_y)}. \tag{4.16}$$

Since the transverse and longitudinal momenta are coupled for the ZGNR, we will not be able to perform the integral above. On the other hand, for the AGNR, the momenta are uncoupled and we may calculate the Green's function above as (for a full derivation, the reader is referred to Appendix A.3)

$$g_n(\vec{r}, \vec{r}\,'; E) = \chi_n(x)\chi_n(x') \begin{pmatrix} \Gamma_n^{AA}(y, y'; E) & \Gamma_n^{AB}(y, y'; E) \\ \Gamma_n^{BA}(y, y'; E) & \Gamma_n^{BB}(y, y'; E) \end{pmatrix}, \tag{4.17}$$

where the transverse wavefunctions are $\chi_n(x) = \sqrt{1/W}\sin\left(\frac{n\pi}{W}x\right)$ and where

$$\Gamma_n^{AA/BB}(y, y'; E) = -i\frac{|E|}{(\hbar v_f)^2}\frac{e^{i\mathrm{sgn}(E)\mu_n(E)|y-y'|}}{\mu_n(E)} \tag{4.18}$$

and

$$\Gamma_n^{AB/BA}(y, y'; E) = -\frac{1}{\hbar v_f}\left[\frac{i\mathrm{sgn}\,(E)\,\kappa_n}{\mu_n} \mp \mathrm{sgn}\left(y - y'\right)\right] e^{i\mathrm{sgn}(E)\mu_n(E)|y-y'|}, \tag{4.19}$$

where

$$\mu_n(E) = \sqrt{\left(\frac{E}{\hbar v_f}\right)^2 - \kappa_n^2}. \tag{4.20}$$

In the case where $\mu_n(E)$ becomes complex (if the mode n is evanescent), we should use that $\mu_n \to i\mathrm{sgn}\,(E)\,|\mu_n|$.

These Green's functions were used in Paper **II** and Paper **IV** to calculate the density of states, and the transmission, through different AGNR's with different impurities. To test the validity, I have performed a tight-binding simulation of an AGNR and extracted the numerical propagators (found using the techniques in Chapter. 3) between the different points shown in Fig. 4.8a. The simulation is done both for a clean ribbon, using 40 evanescent modes, and the results (shown in Fig.4.8b-d) reveal that the match between the Green's functions calculated using the Dirac approximation, and those calculated numerically, is good for low energies.

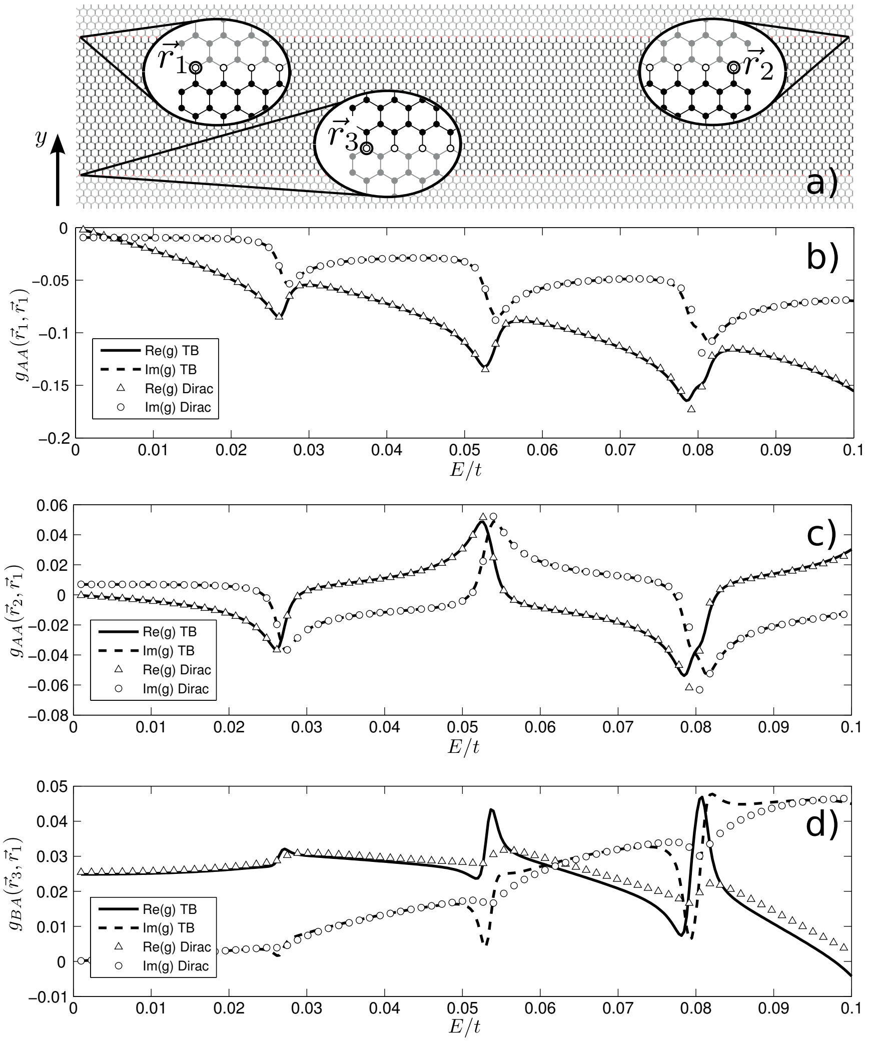

Figure 4.8: Propagators for an AGNR with $N = 101$, calculated both analytically and with numerical tight binding. In all figures, a total of 40 evanescent modes were included, and we see that the Dirac-approximated Green's functions agree fairly well with the tight-binding for low energies.

Chapter 5

Grain boundaries in graphene nanoribbons

In Paper **V** , we investigated how grain boundaries (linear dislocations that separate grains having different lattice orientations) can effect transport properties in graphene, and in particular what happens if such systems are used to perform Quantum Hall measurements. Such a problem formulation excellently fits our numerical methods, but we had to overcome the problem of actually generating an accurate grain boundary with arbitrary misorientation angle between the two graphene grains.

5.1 Grain boundaries and the coincidence site lattice model

As described by Carlsson et al (see [70] and the reference given there), a grain boundary in graphene can be generated by using the *coincidence site lattice model*, or CSL-model. The starting point of this model is to first construct a new graphene unit-cell, which is done by placing two layers of graphene on top of each other. After selecting on of the atoms as a fixed point, we then start to rotate the two lattices relative to each other, and try to find how far we need to go away from the fix-point to find new points that overlap, and in what directions we need to go (see Fig. 5.1a). Using

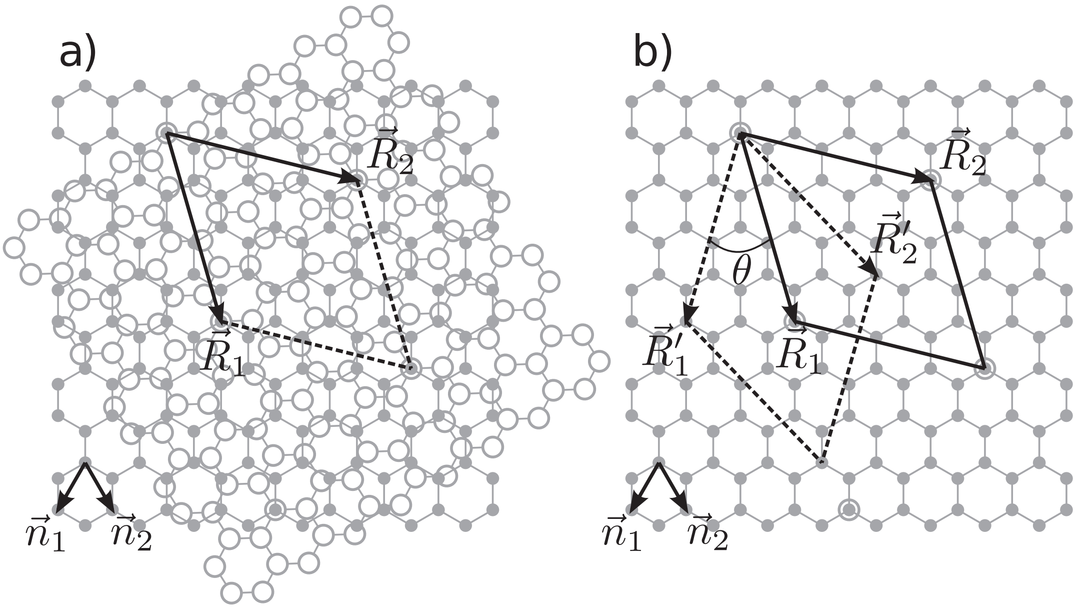

Figure 5.1: The CSL model. In a), the two CSL-lattice vectors span a new CSL-unit cell having. In b), we use the CSL-lattice vectors to extract two unit cells (one from each single layer of graphene), which will allow us to construct a periodic grain boundary by putting the two unit cells togeter. In the system shown, we have used $m = 1, n = 3$, which give $\Sigma = 13$ and $\theta = 32.2°$

the graphene lattice vectors, $\vec{n}_1 = \frac{a_0}{2}(-\sqrt{3}, -3)$ and $\vec{n}_2 = \frac{a_0}{2}(\sqrt{3}, -3)$, we can define a new CSL-unit cell spanned by the CSL-lattice vectors

$$\vec{R}_1 = m\vec{n}_1 + n\vec{n}_2 \quad \text{and} \quad \vec{R}_2 = -n\vec{n}_1 + (m+n)\vec{n}_2, \tag{5.1}$$

where m and n are integer indices. These vectors will point directly at the neareast overlapping atoms, and they define a new unit-cell having area

$$\Omega_{CSL} = |\vec{R}_1 \times \vec{R}_2| = |n^2 + m(m+n)||\vec{n}_1 \times \vec{n}_2|. \tag{5.2}$$

To compare this area to the one of graphene, $\Omega = |\vec{n}_1 \times \vec{n}_2|$, we define the quota

$$\Sigma = \Omega_{CSL}/\Omega = m^2 + n^2 + mn, \tag{5.3}$$

which, together with the indices m and n allows us to classify series of different grain boundaries. The example in Fig.5.1 uses $m = 1$, $n = 3$ and

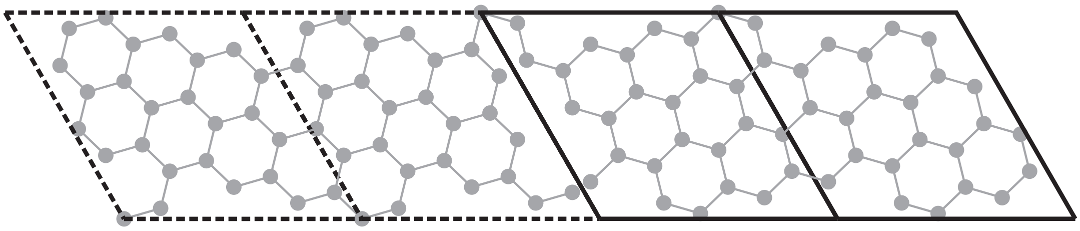

Figure 5.2: Grain boundary supercell, before force-field relaxation

have $\Sigma = 13$. The misorientation angle (i.e., the angle the two sheets of graphene are rotated relative each other), is $\theta = 23.2°$.

When we have found the CSL-unit cell, we can extract one unit cell from each single layer of graphene, as shown in Fig.5.1b. One cell is found directly using the CSL-vectors $\vec{R}_1$ and $\vec{R}_2$, while the other one is found by rotating these vectors θ relative to the others, giving a unit cell spanned by the vectors $\vec{R}'_1$ and $\vec{R}'_2$.

In figure 5.2, we have taken the two unit cells shown in 5.1b, and rotated them so that they fit together. In the figure, two of the cells drawn with solid black lines (corresponding to $\vec{R}_i$) are first joined together, and then positioned next to two of the cells drawn with dashed lines (corresponding to $\vec{R}'_i$). The grain boundary is formed between the two different kind of cells.

As seen in the figure, the grain oundary is still not very good looking. To solve this problem, one has to rely on more advanced methods such as force-field-relaxation, which wiggles the atoms around until the total energy of the system is minimized. It may also be required to shift the different kind of cells relative each other (along the grain boundary). This procedure has been performed using the software Materials Studio [71], and the result is shown in Fig. 5.3. Now, the grain boundary looks nice, and if we place many of the new supercells together we get an extended grain boundary supercell as shown in Fig. 5.4, a grain boundary made up from a repeating pattern of pentagons and heptagons.

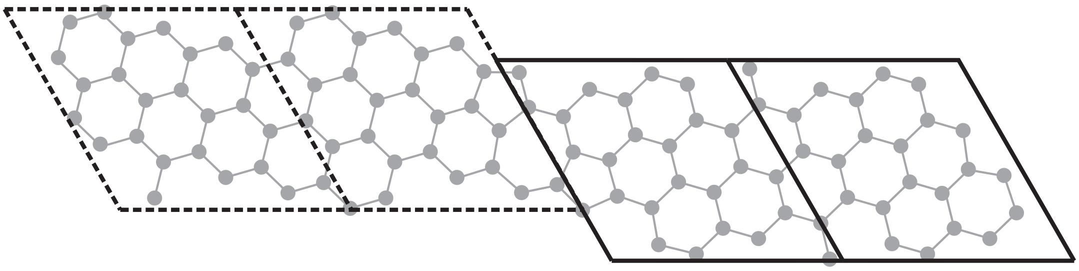

Figure 5.3: Grain boundary supercell, after force-field relaxation and a relative shift along the grain boundary

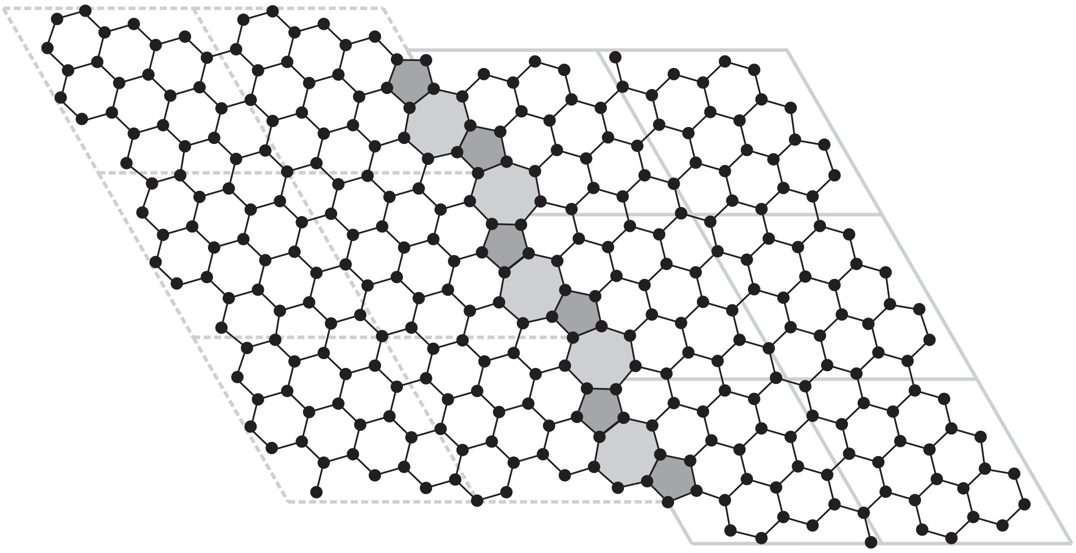

Figure 5.4: Extended grain boundary supercell in graphene

5.2 Quantum Hall measurements

As stated in the beginning of this chapter, we are interested in how the grain boundaries effects Quantum Hall measurements. The (integer) Quantum Hall Effect (QHE) can easiest, with a bit of hand-waving, be described by looking at Fig. 5.5. Here, a two-dimensional slab of material is placed in a magnetic field $\vec{B}$, aligned perpendicularly to the plane of the slab. Using the infamous *right-hand rule*, we know that an electron subject to a magnetic

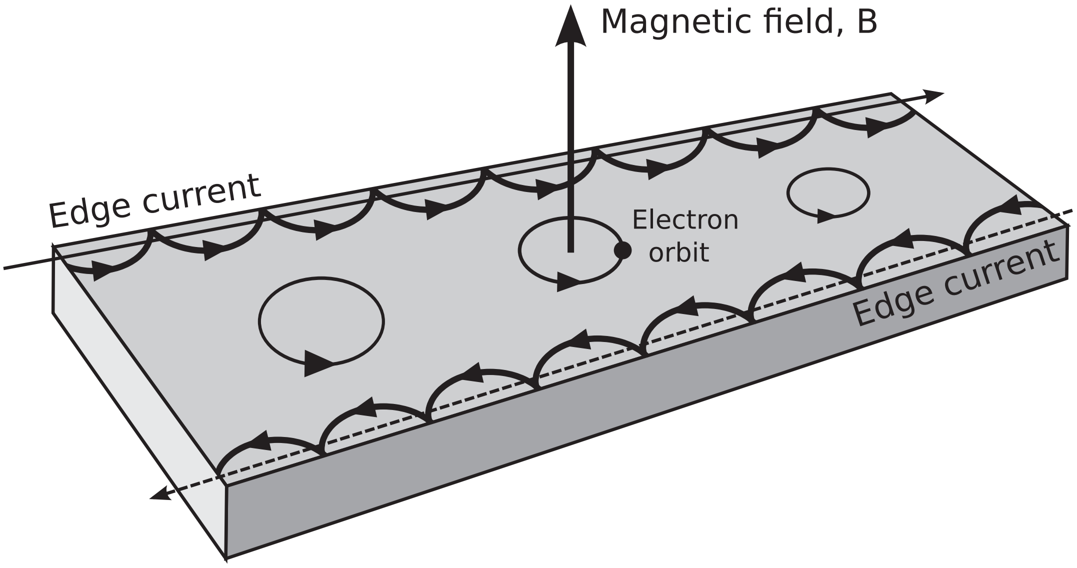

Figure 5.5: A simple schematic picture illustrating the Quantum Hall Effect in two-dimensional systems in a magnetic field.

field will bend to the left if the magnetic field is aligned as in the figure. If the field is strong enough, the electrons will bend enough as to form closed orbitals. This is true at least for the electrons located in the middle of the slab, far away from the edges. At the edges, however, an electron will not be able to complete a full orbit (since it is not allowed to "fall off the edge"). Instead, the electron will follow so scalled *skipping orbits* along the edges. Due to the magnetic field, and the geometric nature of the problem (that all electrons rotate in the same direction), electrons travelling along the edges will only be able to propagate in a certain direction, along the edge, and this direction will be different depending on if the electron is travelling along the left or right edge (as shown in the figure). These states, called *edge states*, only exists at the edges of the sample, and if one attaches contacts to the slab and tries to run current through it, only the electrons in these edge states will be involved in the conductance (since the bulk electrons are occupied with going around in circles). The word "quantum" enters the title since the energy of the orbitals will be quantized [72, 73], according to $E_n = \hbar\omega_c(n + 1/2)$, where the *cyclotron frequency* is defined as $_c = e|B|/m$, and the orbital radius are related to the *magnetic length* $l_B = \sqrt{\hbar/(e|B|)}$.

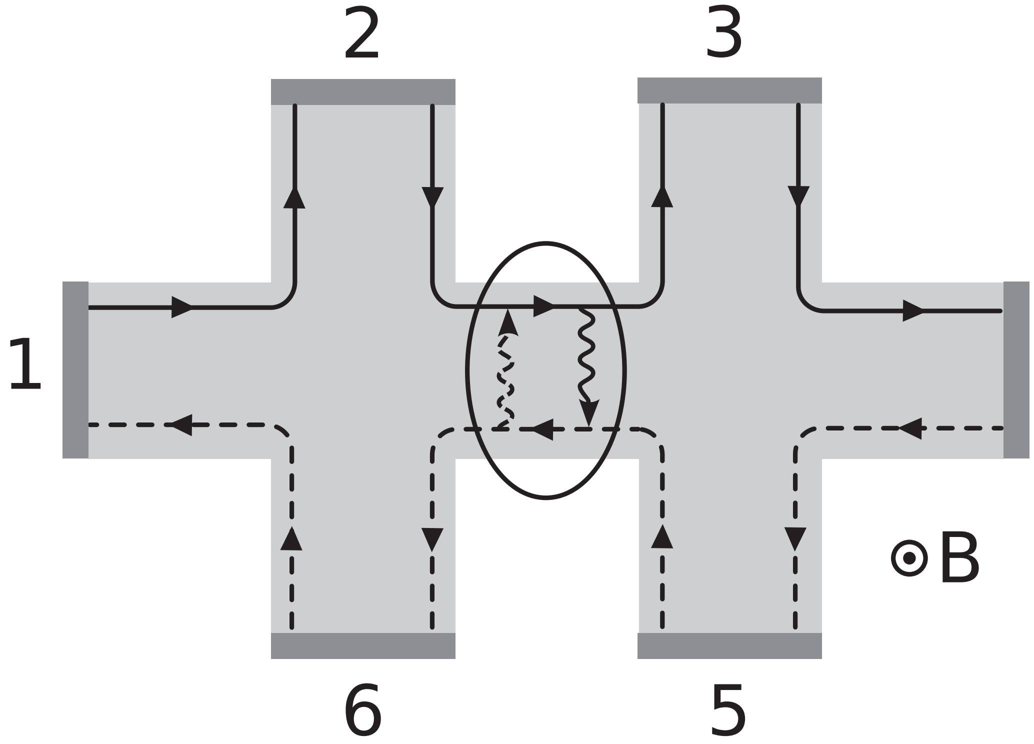

Figure 5.6: Quantum Hall bar measurement setup. For clean material, the current only flows along the edges. Impurities or defects, such as grain boundaries, may open channels connecting opposite edges, allowing the electron current to take short-cuts across the sample, as shown inside the dashed oval.

When doing Quantum Hall measurements, the slab discussed earlier is formed into the shape shown in Fig. 5.6, and contacts are attached to the different arms. If the material used is clean (free from e.g. impurities), the presence of the edge states will make the current only run along the edges as is seen in the figure. The specific geometry is usually referred to as a *Quantum Hall bar*. If one injects a current I_1 into contact 1 (in Fig. 5.6), and measures the voltage V_{26} over contacts 2 and 6, one can extract the *transversal* resistivity $\rho_{xy} = V_{26}/I_1$. If one uses the same current, but instead measures the voltage V_{23} across contacts 2 and 3, one would measure the *longitudinal* resistivity $\rho_{xx} \propto V_{23}/I_1$.

Since current is only allowed to travel along the edges, and since the direction of current is fixed, one expects current to flow without dissipation along the edges, since there are no way for them to scatter back except if they manage to move to the opposite edge. Thus, if contact 4 is grounded, one would expect to measure the same voltage V on the contacts 1, 2 and 3, while zero voltage would be measured on the contacts 4, 5 and 6. The longitudinal resistance, ρ_{xx} would then be zero since $V_{23} = V_2 - V_3 = V - V = 0$. The current flowing along the edges is carried by the edge states, and depending on how many modes (or edge channels) that are open this current will be quantized as $I_1 = nG_cV_1$, where $G_c = e^2/h$ is the *Hall conductivity*, and n an integer. The resistivity $\rho_{xy} \propto V_{26}/I_1 = V/I_1 = 1/(nG_c)$ will then also be quantized, since n is an integer.

5.3 Attenuation of the Quantum Hall Effect

At the end of this chapter, we now put the two previous sections together trying to answer one currently important question: why does the Hall Effect, when measured in graphene, break down? With "break down", I here mean that the predicted features discussed recently, the plateaus and quantization of ρ_{xy}, and the zero value of ρ_{xx} on said plateaus, is not observed experimentally (for a nice review, see [74]). As we have seen in the previous section, one reason may be that there is something in the experimental sample that connects two opposite edges together, allowing the electrons to scatter back, and thus causing the nice quantization of the current to break down. As we have shown in Paper **V** , a grain boundary in the graphene, extending from one edge to the other, may be exactly the underlying reasons (among others [75, 76]) for the experimental observations and then especially in graphene grown using CVD (chemical vapour deposition) on for, e.g., cupper, where the formation of graphene grain boundaries is very common (see, e.g., [77]). If a metallic state is formed along the grain boundary, the grain boundary works as a channel connecting the two edges together, and the interested reader is referred to the attached Paper **V** for more information and references.

Chapter 6

Summary

In this thesis we have studied transport related phenomena in the material graphene, using both analytical analysis and numerical simulations based on recursive, atomistic tight-binding simulations. We have shown how graphene, due to its two-dimensional structure, can serve as contact material for molecules, and how a graphene nanogap bridged by such molecules can result in a transistor effect if the system is backgated. We have also shown that edge roughness of the graphene leads, and impurities, do not cancellate this effect.

By investigating, both analytically and numerically, how impurities in nanoribbons interplay with the effects of size quantization, we have shown how the characteristic features of the Fourier transformed local density of states can be understood in terms of electrons scattering between different transverse modes (sub-bands). Using the same system setup, we have also analyzed how the impurities present in the ribbon can effect transport through the ribbon, and pointed out how quasi-bound states at the impurity causes characteristic dips in the transmission function where a full quantum of conductance is lost, and that, at the opening of a new propagating channel, this loss is completely gone rendering a perfectly conducting channel again.

By constructing, simulating and analyzing transverse grain boundaries in graphene ribbons, we have shown how such grain boundaries can render a metallic state, actively creating a shortcut between the edges of the ribbons.

This added channel, which allows electrons to move from one edge to another, even in a magnetic field when electrons otherwise are forced to travel only in edge channels, can attenuate and even destroy the quantum Hall effect. This may explain the origin of non-zero longitudinal resistivity, and non-quantized transverse resistivity, in quantum Hall bar measurements, especially in graphene grown on metal substrates where grain boundaries are more common.

We have also contributed a pedagogical description of how recursive tight-binding methods may be used to effeciently simulate quantum coherent electron transport. As promised in the introduction, it is hoped that the chapters in this thesis have given the reader a better understanding, and a general basic introduction to, the field of graphene, and that the reading of the attached papers are thus facilitated.

The numerical framework we have implemented and/or developed are flexible, and with the possibility to add extra degrees of inner freedom it is well suited for future studies of more complex systems and physics, such as spin or superconductivity.

Acknowledgements

During the time I have spent as a Ph.D. student (and a Master's student) at Chalmers, MC2 and the Applied Quantum Physics Laboratory, I have come into contact with an extensive number of people to whom I am grateful.

First of all, I would like to thank my supervisor, Tomas Löfwander, for all of our discussions, for him always taking his time to answer my many questions, and for all other help (be it with numerics, physics or life in general) I have received. I am also thankful to the rest of the senior staff at the laboratory: to Vitaly Shumeiko for his guidance during my Master's thesis and his inspirational way of discussing physics, and to Mikael Fogelström, Göran Johansson and the groups latest senior member, Janine Splettstoesser, for all creating a nice and intellectual environment to work in. I have enjoyed the company of my current, and previous, office buddies: Yevgeneiy, Ian, Joel and Cecilia, and all of the other current and former postdocs and PhD students I have had the pleasure to share both work-related and private moments with, including Markku, Juha, Oleksii, Daniel, Tobias, Sankar, Mikael, Anton, Jens, Jens again, Lars and Hector. I wish you all the best, and a big good luck with your future careers! I would also like to thank the whole administrative staff of MC2, and especially Jeanette and Emma.

To my long-term friend Erik: I have enjoyed our holidays, our dinners and I wish you all the best in Germany and wherever the future takes you, and I expect us to stay in contact even if I now am heading away from the world of academia. Finally, I would like to thank my beloved family for always supporting me, and, Elisabeth, I love you and look forward to every second of our future life together (without having to travel back and forth every weekend!).

Appendix A

Wavefunctions and electron propagators in graphene nanoribbons

A.1 Zigzag nanoribbons (ZGNR)

Let $\kappa_y \to -i\partial_y$. The boundary condition is that $\Psi_A(x, y = 0) = \Psi_B(x, y = W) = 0$, and we can rewrite the pseudo-spinors as

$$\vec{\psi}^{\nu}(\vec{r}) = e^{i\kappa_x x}\vec{\phi}^{\nu}(y) = e^{i\kappa_x x}\begin{pmatrix}\phi_A^{\nu}(y)\\ \phi_B^{\nu}(y)\end{pmatrix} \tag{A.1}$$

which, after inserting in (4.1) and applying the boundary condition, gives us that

$$e^{iKx}e^{i\kappa_x x}\phi_A^{+}(0) + e^{-iKx}e^{i\kappa_x x}\phi_A^{-}(0) = 0, \tag{A.2}$$

$$e^{iKx}e^{i\kappa_x x}\phi_B^{+}(W) + e^{-iKx}e^{i\kappa_x x}\phi_B^{-}(W) = 0. \tag{A.3}$$

By inspection, we find that the two equations (A.2) and (A.3) are solved if $\phi_A^{\nu}(0) = \phi_B^{\nu}(W) = 0$. The transverse functions should also be eigenfunctions of the Dirac Hamiltonian:

$$h^{\nu}(\vec{\kappa})\vec{\phi}^{\nu}(y) = \epsilon(\vec{\kappa})\vec{\phi}^{\nu}(y), \tag{A.4}$$

or,

$$\hbar v_f \begin{pmatrix} 0 & \nu\kappa_x - \partial_y \\ \nu\kappa_x + \partial_y & 0 \end{pmatrix} \begin{pmatrix} \phi_A^\nu(y) \\ \phi_B^\nu(y) \end{pmatrix} = \epsilon(\vec{\kappa}) \begin{pmatrix} \phi_A^\nu(y) \\ \phi_B^\nu(y) \end{pmatrix}. \tag{A.5}$$

This gives us two coupled equations

$$\hbar v_f (\nu\kappa_x - \partial_y)\phi_B^\nu(y) = \epsilon(\vec{\kappa})\phi_A^\nu(y) \tag{A.6}$$

and

$$\hbar v_f (\nu\kappa_x + \partial_y)\phi_A^\nu(y) = \epsilon(\vec{\kappa})\phi_B^\nu(y). \tag{A.7}$$

Multiply the second equation with $\hbar v_f(\nu\kappa_x - \partial_y)$ to get

$$\hbar^2 v_f^2 (\kappa_x^2 - \partial_y^2)\phi_A^\nu(y) = \epsilon(\vec{\kappa}) \underbrace{\hbar v_f (\nu\kappa_x - \partial_y)\phi_B^\nu(y)}_{=\epsilon(\vec{\kappa})\phi_A^\nu(y)} = \epsilon^2(\vec{\kappa})\phi_A^\nu(y). \tag{A.8}$$

This is solved by making the ansatz

$$\phi_A^\nu(y) = C_A^\nu e^{i\kappa_n y} + D_A^\nu e^{-i\kappa_n y} \tag{A.9}$$

leading to

$$\hbar^2 v_f^2 (\kappa_x^2 - \partial_y^2)\phi_A^\nu(y) = \hbar^2 v_f^2 (\kappa_x^2 + \kappa_n^2)\phi_A^\nu(y) = \epsilon^2(\vec{\kappa})\phi_A^\nu(y), \tag{A.10}$$

and $\epsilon(\vec{\kappa}) = \lambda\hbar v_f\sqrt{\kappa_x^2 + \kappa_n^2}$ where $\lambda = \pm 1$. The first boundary condition, $\phi_A^\nu(0) = 0$, tells us that

$$\phi_A^\nu(0) = C_A^\nu + D_A^\nu = 0 \rightarrow D_A^\nu = -C_A^\nu, \tag{A.11}$$

so that

$$\phi_A^\nu(y) = C_A^\nu \left(e^{i\kappa_n y} - e^{-i\kappa_n y}\right) = 2iC_A^\nu \sin(\kappa_n y). \tag{A.12}$$

The B-component is found from (A.7),

$$\begin{aligned} \phi_B^\nu(y) &= \frac{\hbar v_f}{\epsilon(\vec{\kappa})}(\nu\kappa_x + \partial_y)\,\phi_A^\nu(y) \\ &= \frac{\hbar v_f C_A^\nu}{\epsilon(\vec{\kappa})}\left[(\nu\kappa_x + i\kappa_n)e^{i\kappa_n y} - (\nu\kappa_x - i\kappa_n)e^{-i\kappa_n y}\right] \\ &= \{\text{if } \kappa_n \text{ is real}\} = 2i\lambda C_A^\nu \sin\left[\kappa_n y + \theta_\nu(\vec{\kappa})\right], \end{aligned} \tag{A.13}$$

where $\theta_\nu(\vec{\kappa}) = \arg(\nu\kappa_x + i\kappa_n)$.

Using the second boundary condition, $\phi_B^\nu(W) = 0$, we find that

$$e^{2i\kappa_n W} = \frac{\nu\kappa_x - i\kappa_n}{\nu\kappa_x + i\kappa_n}, \tag{A.14}$$

which we can rewrite as

$$\nu\kappa_x = -\frac{\kappa_n}{\tan(\kappa_n W)}. \tag{A.15}$$

We can also have solutions where κ_n is imaginary, i.e., $\kappa_n = iq_n$ and $E = \hbar v_f\sqrt{\kappa_x^2 - q_n^2}$, which changes equation (A.15) to

$$\nu\kappa_x = -\frac{q_n}{\tanh(q_n W)}. \tag{A.16}$$

The solutions are localized edge-states.

We note that, for Zigzag ribbons, the transversal momentum κ_n is depending on the longitudinal momentum as seen in equations (A.15) and (A.16). None of these equations allow for analytical solutions, but we can always solve them numerically.

Normalization

The coefficient C_A^ν can be found by requiring that

$$\int_0^W dy\ |\phi_A^\nu(y)|^2 = \frac{1}{4}, \tag{A.17}$$

which gives us the wanted total of unity if we sum the wavefunctions over both valleys and both sublattices. We find that, for real κ_n,

$$\begin{aligned}\int_0^W dy\ |\phi_A^\nu(y)|^2 &= 4C_A^\nu \int_0^W dy\ \sin^2(\kappa_n y) = \\ &= \frac{(2C_A^\nu)^2}{2}\int_0^W dy\ [1-\cos(2\kappa_n y)] = \dots \\ &= (C_A^\nu)^2\,\frac{2\kappa_n W - \sin(2\kappa_n W)}{\kappa_n} = \frac{1}{4},\end{aligned} \tag{A.18}$$

or, that

$$C_A^\nu = C_A^\nu(\kappa_n) = \frac{1}{2}\sqrt{\frac{\kappa_n}{2\kappa_n W - \sin(2\kappa_n W)}}. \tag{A.19}$$

For imaginary $\kappa_n = iq_n$, we have that

$$C_\nu^A(q_n) = \frac{1}{2}\sqrt{\frac{q_n}{\sinh(2q_n W) - 2q_n W}}. \tag{A.20}$$

A.2 Armchair nanoribbons (AGNR)

Let $\kappa_x \to -i\partial_x$. The boundary condition is that $\vec{\Psi}(x = 0, y) = \vec{\Psi}(x = W, y) = 0$, that is, both sublattice components must vanish on both edges.

We rewrite the spinor as

$$\vec{\psi}^\nu(\vec{r}) = e^{i\kappa_y y}\vec{\phi}^\nu(x) = e^{i\kappa_y y}\begin{pmatrix}\phi_A^\nu(x)\\ \phi_B^\nu(x)\end{pmatrix} \tag{A.21}$$

and

$$-i\hbar v_f \begin{pmatrix}0 & \nu\partial_x + \kappa_y\\ \nu\partial_x - \kappa_y & 0\end{pmatrix}\begin{pmatrix}\phi_A^\nu(x)\\ \phi_B^\nu(x)\end{pmatrix} = \epsilon(\vec{\kappa})\begin{pmatrix}\phi_A^\nu(x)\\ \phi_B^\nu(x)\end{pmatrix}. \tag{A.22}$$

After insertion into (4.1), and after applying the boundary condition, we get that

$$\vec{\psi}^+(0) + \vec{\psi}^-(0) = 0, \tag{A.23}$$

$$e^{iKW}\vec{\psi}^+(W) + e^{-iKW}\vec{\psi}^-(W) = 0. \tag{A.24}$$

Repeating the ansatz, $\phi_A^\nu(x) = C_A^\nu e^{i\kappa_n x} + D_A^\nu e^{-i\kappa_n x}$, we get that

$$C_A^+ + D_A^+ + C_A^- + D_A^- = 0, \tag{A.25}$$

$$e^{i(K+\kappa_n)W}C_A^+ + D^{i(K-\kappa_n)W}D_A^+ + e^{-i(K-\kappa_n)W}C_A^- + e^{-i(K+\kappa_n)W}D_A^- = 0. \tag{A.26}$$

By inspection, one solution is to set $C_A^+ = -D_A^-$ and $C_A^- = D_A^+ = 0$, leading to

$$C_A^+\left(e^{i(K+\kappa_n)W} - e^{-i(K+\kappa_n)W}\right) = 2iC_A^+\sin\left[(K+\kappa_n)W\right] = 0. \tag{A.27}$$

We thus find that the condition for κ_n is that $(K+\kappa_n)W = n\pi$, or

$$\kappa_n = \frac{n\pi}{W} - K = \frac{n\pi}{W} - \frac{4\pi}{3a}. \tag{A.28}$$

and that the energy dispersion is $\epsilon(\vec{\kappa}) = \pm\hbar v_f\sqrt{\kappa_y^2 + \kappa_n^2}$. We have that

$$\phi_A^\nu(x) = \nu C_A^\nu e^{i\nu\kappa_n x}, \tag{A.29}$$

and, following the same procedure as for the zigzag ribbon, we find that

$$\begin{aligned}\phi_B^{\nu}(x) &= \frac{-i\hbar v_f}{\epsilon(\vec{\kappa})}(\nu\partial_x - \kappa_y)\phi_A^{\nu}(x) \\ &= \frac{-i\nu\hbar v_f C_A^{\nu}}{\epsilon(\vec{\kappa})}(i\kappa_n - \kappa_y)e^{i\nu\kappa_n x} \\ &= i\lambda\nu C_A^{\nu} e^{i\theta(\vec{\kappa})} e^{i\nu\kappa_n x},\end{aligned} \tag{A.30}$$

where $\theta(\vec{\kappa}) = \arg(\kappa_y - i\kappa_n)$.

Normalization

Due to the symmetry between the A- and B-lattice, we require that the wavefunction on each sublattice is normalized so that

$$\int_0^W dx\, \left|\Psi_{A/B}(x)\right|^2 = 4|C_A^{\nu}|^2 \int_0^W dx\ \sin^2\left(\frac{n\pi}{W}x\right) = 2|C_A^{\nu}|^2 W = \frac{1}{2}, \tag{A.31}$$

from which we see that $C_A^{\nu} = \sqrt{1/4W}$.

A.3 Green's functions

Look at the armchair case, where we can find transverse (κ_n) momentum independent of the longitudinal (κ_y) momentum. Using the Lehmann representation [78, 79], the electron propagator in mode n, energy E, from point $\vec{r}\,'$ to $\vec{r}$ is given by

$$\begin{aligned}g_n(\vec{r},\vec{r}\,';E) &= \sum_{\lambda=\pm 1}\int_{-\infty}^{\infty}\frac{d\kappa_y}{2\pi}\frac{\vec{\Psi}(\vec{r})\vec{\Psi}^{\dagger}(\vec{r}\,')}{E^+ - \epsilon_{n\lambda}(\kappa_y)} \\ &= \sum_{\lambda=\pm 1}\int_{-\infty}^{\infty}\frac{d\kappa_y}{2\pi}\frac{1}{E^+ - \epsilon_{n\lambda}(\kappa_y)}\begin{pmatrix}\Psi_A(\vec{r})\Psi_A^*(\vec{r}\,') & \Psi_A(\vec{r})\Psi_B^*(\vec{r}\,') \\ \Psi_B(\vec{r})\Psi_A^*(\vec{r}\,') & \Psi_B(\vec{r})\Psi_B^*(\vec{r}\,')\end{pmatrix},\end{aligned} \tag{A.32}$$

where $E^+ = E + i\eta$, $\epsilon_{n\lambda}(\kappa_y) = \hbar v_f\sqrt{\kappa_y^2 + \kappa_n^2}$ and $\kappa_n = n\pi/W - K$. If we separate this expression into an x- and y-dependent part, we have that

$$\mathbf{g}_n(\vec{r}, \vec{r}'; E) = \frac{1}{2\pi W}\sin\left(\frac{n\pi}{W}x\right)\sin\left(\frac{n\pi}{W}x'\right)\begin{pmatrix} g_n^{AA}(y, y'; E) & g_n^{AB}(y, y'; E) \\ g_n^{BA}(y, y'; E) & g_n^{BB}(y, y'; E) \end{pmatrix}. \tag{A.33}$$

Diagonal parts

The diagonal (y-dependent) parts of equation (A.33) are

$$\begin{aligned} g_n^{AA}(y, y'; E) &= \int_{-\infty}^{\infty} d\kappa_y \frac{e^{i\kappa_y(y-y')}(\kappa_y^2 + \kappa_n^2)}{\kappa_y^2 + \kappa_n^2} \sum_{\lambda=\pm 1} \frac{\lambda^2}{E^+ - \epsilon_{n\lambda}(\kappa_y)} \\ &= 2E^+ \int_{-\infty}^{\infty} d\kappa_y \frac{e^{i\kappa_y(y-y')}}{(E^+)^2 - (\hbar v_f)^2(\kappa_y^2 + \kappa_n^2)} \\ &= -\frac{2E^+}{(\hbar v_f)^2}\int_{-\infty}^{\infty} d\kappa_y \frac{e^{i\kappa_y(y-y')}}{\kappa_y^2 - \underbrace{\left[(\tilde{E}^+)^2 - \kappa_n^2\right]}_{=(\mu_n^+)^2}} \\ &= -\frac{2E^+}{(\hbar v_f)^2}\underbrace{\int_{-\infty}^{\infty} d\kappa_y \frac{e^{i\kappa_y(y-y')}}{(\kappa_y + \mu^+)(\kappa_y - \mu_n^+)}}_{=I^n(y,y';E)} \end{aligned} \tag{A.34}$$

and

$$\begin{aligned} g_n^{BB}(y, y'; E) &= \int_{-\infty}^{\infty} d\kappa_y \; e^{i\kappa_y(y-y')} \sum_{\lambda=\pm 1} \frac{1}{E^+ - \epsilon_{n\lambda}(\kappa_y)} \\ &= ... \\ &= g_n^{AA}(y, y'; E), \end{aligned} \tag{A.35}$$

where $\tilde{E}^+ = E^+/(\hbar v_f)$.

To solve the integral in the expression for $g_n^{AA/BB}(y, y'; E)$, we first note

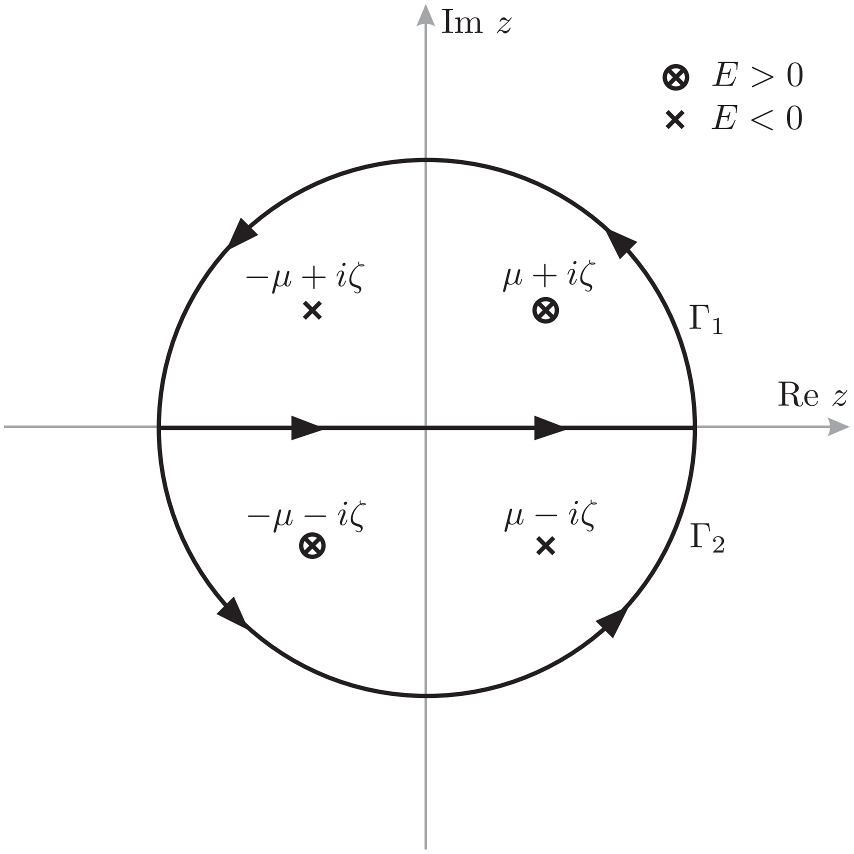
Im z
$E > 0$
$E < 0$
$-\mu + i\zeta$
$\mu + i\zeta$
Γ_1
Re z
$-\mu - i\zeta$
$\mu - i\zeta$
Γ_2

Figure A.1: Integration contour(s) in the complex plane.

that

$$\begin{aligned}\mu_n^+ &= \sqrt{(\tilde{E}^+)^2 - \kappa_n^2} = \sqrt{\tilde{E}^2 - \kappa_n^2 + 2i\tilde{E}\tilde{\eta} + O(\tilde{\eta}^2)} \\ &\approx \underbrace{\sqrt{\tilde{E}^2 - \kappa_n^2}}_{=\mu_n} \sqrt{1 + i\frac{2\tilde{E}\tilde{\eta}}{\tilde{E}^2 - \kappa_n^2}} \approx \mu_n + i\mathrm{sgn}\,(E)\,\zeta.\end{aligned} \tag{A.36}$$

This tells us that the integrand has poles (let $\kappa_y \to z$) at $z = \pm(\mu_n + i\mathrm{sgn}\,(E)\,\zeta)$, and we integrate using the contours shown in figure A.1. The residues of the four possible poles are given by

$$\begin{aligned}
\mathrm{Res}(z=\mu_n+i\zeta) &= \frac{e^{i\mu_n(y-y')-\zeta(y-y')}}{2(\mu_n+i\zeta)}, && \text{(A.37)}\\
\mathrm{Res}(z=-\mu_n-i\zeta) &= \frac{e^{-i\mu_n(y-y')+\zeta(y-y')}}{-2(\mu_n+i\zeta)}, && \text{(A.38)}\\
\mathrm{Res}(z=\mu_n-i\zeta) &= \frac{e^{i\mu_n(y-y')+\zeta(y-y')}}{2(\mu_n-i\zeta)}, && \text{(A.39)}\\
\mathrm{Res}(z=-\mu_n+i\zeta) &= \frac{e^{-i\mu_n(y-y')-\zeta(y-y')}}{-2(\mu_n-i\zeta)}. && \text{(A.40)}
\end{aligned}$$

If $y - y' > 0$, we integrate along the contour Γ_1 in the upper half plane in figure A.1 and we find that

$$I^n(y,y';E) = i\mathrm{sgn}\,(E)\,\pi\frac{e^{i\mathrm{sgn}(E)\mu_n(y-y')-\zeta(y-y')}}{\mu_n+i\mathrm{sgn}\,(E)\,\zeta}. \tag{A.41}$$

If $y - y' < 0$, we use the lower contour Γ_2 instead and

$$I^n(y,y';E) = i\mathrm{sgn}\,(E)\,\pi\frac{e^{-i\mathrm{sgn}(E)\mu_n(y-y')+\zeta(y-y')}}{\mu_n+i\mathrm{sgn}\,(E)\,\zeta}. \tag{A.42}$$

In general, we have that

$$I^n(y,y';E) = i\mathrm{sgn}\,(E)\,\pi\frac{e^{i\mathrm{sgn}(E)\mu_n|y-y'|-\zeta|y-y'|}}{\mu+i\mathrm{sgn}\,(E)\,\zeta}, \tag{A.43}$$

and

$$g_n^{AA/BB}(y,y';E) = -2\pi i\mathrm{sgn}\,(E)\,\frac{(E+i\eta)}{(\hbar v_f)^2}\,\frac{e^{i\mathrm{sgn}(E)\mu_n|y-y'|-\zeta|y-y'|}}{\mu_n+i\mathrm{sgn}\,(E)\,\zeta}. \tag{A.44}$$

The diagonal elements of the full unperturbed Green's function are therefore, in the limit where $\eta,\zeta\to 0^+$,

$$g_n(\vec{r},\vec{r}\,';E)^{AA/BB} = -i\frac{|E|}{W(\hbar v_f)^2}\sin\left(\frac{n\pi}{W}x\right)\sin\left(\frac{n\pi}{W}x'\right)\frac{e^{i\mathrm{sgn}(E)\mu_n|y-y'|}}{\mu_n}. \tag{A.45}$$

Off-diagonal parts

The off-diagonal (y-dependent) parts of equation (A.33) are

$$\begin{aligned} g_n^{AB}(y,y';E) &= -i\int_{-\infty}^{\infty} d\kappa_y\; e^{i\kappa_y(y-y')}\frac{(\kappa_y+i\kappa_n)}{\sqrt{\kappa_y^2+\kappa_n^2}}\sum_{\lambda=\pm1}\frac{\lambda}{E^+-\epsilon_{n\lambda}(\kappa_y)} \\ &= -i\int_{-\infty}^{\infty} d\kappa_y\; e^{i\kappa_y(y-y')}\frac{(\kappa_y+i\kappa_n)}{\sqrt{\kappa_y^2+\kappa_n^2}}\frac{2\hbar v_f\sqrt{\kappa_y^2+\kappa_n^2}}{(E^+)^2-(\hbar v_f)^2(\kappa_y^2+\kappa_n^2)} \\ &= \frac{2i}{\hbar v_f}\int_{-\infty}^{\infty} d\kappa_y\; e^{i\kappa_y(y-y')}\frac{(\kappa_y+i\kappa_n)}{(\kappa_y-\mu_n^+)(\kappa_y+\mu_n^+)} \\ &= \frac{2i}{\hbar v_f}\left[i\kappa_n I^n(y,y';E) + \underbrace{\int_{-\infty}^{\infty} d\kappa_y \frac{\kappa_y e^{i\kappa_y(y-y')}}{(\kappa_y-\mu_n^+)(\kappa_y+\mu_n^+)}}_{=J^n(y,y';E)}\right]. \end{aligned} \tag{A.46}$$

The integral $J^n(y,y';E)$ is evaluated using the same contour as earlier. Since the poles are located at the same places, the residues will be

$$\mathrm{Res}(z=\mu_n+i\zeta) = \frac{e^{i\mu_n(y-y')-\zeta(y-y')}}{2}, \tag{A.47}$$

$$\mathrm{Res}(z=-\mu_n-i\zeta) = \frac{e^{-i\mu_n(y-y')+\zeta(y-y')}}{2}, \tag{A.48}$$

$$\mathrm{Res}(z=\mu_n-i\zeta) = \frac{e^{i\mu_n(y-y')+\zeta(y-y')}}{2}, \tag{A.49}$$

$$\mathrm{Res}(z=-\mu_n+i\zeta) = \frac{e^{-i\mu_n(y-y')-\zeta(y-y')}}{2}. \tag{A.50}$$

If $y-y'>0$, integrating along the upper contour gives us that

$$J^n(y,y';E) = i\pi e^{i\mathrm{sgn}(E)\mu_n(y-y')-\zeta(y-y')}, \tag{A.51}$$

and if $y-y'<0$, we find (using the lower contour) that

$$J^n(y,y';E) = -i\pi e^{-i\mathrm{sgn}(E)\mu_n(y-y')+\zeta(y-y')}. \tag{A.52}$$

In general,

$$J^n(y,y';E) = i\mathrm{sgn}\left(y-y'\right)\pi e^{i\mathrm{sgn}(E)\mu_n|y-y'|-\zeta|y-y'|} \tag{A.53}$$

and the off-diagonal parts are

$$g_n^{AB/BA}(y,y';E) = \frac{2\pi i}{\hbar v_f}\left[-\mathrm{sgn}\left(E\right)\frac{\kappa_n}{\mu_n + i\mathrm{sgn}\left(E\right)\zeta} \pm i\mathrm{sgn}\left(y-y'\right)\right] \times e^{i\mathrm{sgn}(E)\mu_n|y-y'|-\zeta|y-y'|}, \tag{A.54}$$

and, in the limit $\eta, \zeta \to 0^+$, we find that the full, unperturbed, off-diagonal propagator elements are

$$g_n^{AB/BA}(y,y';E) = -\frac{1}{W\hbar v_f}\left[\frac{i\mathrm{sgn}\left(E\right)\kappa_n}{\mu_n} \pm \mathrm{sgn}\left(y-y'\right)\right] \times \sin\left(\frac{n\pi}{W}x\right)\sin\left(\frac{n\pi}{W}x'\right)e^{i\mathrm{sgn}(E)\mu_n|y-y'|}. \tag{A.55}$$

Appendix B

Recursive method for the computation of lead Green's functions

When calculating the lead/contact surface Green's functions (the starting point for the knitting algorithm), we use a version of the slice-by-slice method where we, instead of adding a single slice at a time, double the amount of slices for each step. This improves the convergence exponentially, and in a couple of runs, we can accurately simulate surface Green's functions of semi-infinite ribbons (leads).

The different steps are shown in Fig. B.1. The example is using a rectangular lattice, but works just as well for any type of ribbon that can be divided into repeating unit-cells (or slices) in the longitudinal direction.

Step 1. Calculate g for a single slice, $g_{aa} = (E + i\eta - H_0)^{-1}$.

Step 2. First doubling. Set $g_{bb} = g_{aa}$ and calculate

$$G_{aa} = (1 - g_{aa}V_{ab}g_{bb}V_{ba})^{-1}g_{aa}, \tag{B.1}$$

$$G_{bb} = (1 - g_{bb}V_{ba}g_{aa}V_{ab})^{-1}g_{bb}, \tag{B.2}$$

$$G_{ab} = g_{aa}V_{ab}G_{bb}, \tag{B.3}$$

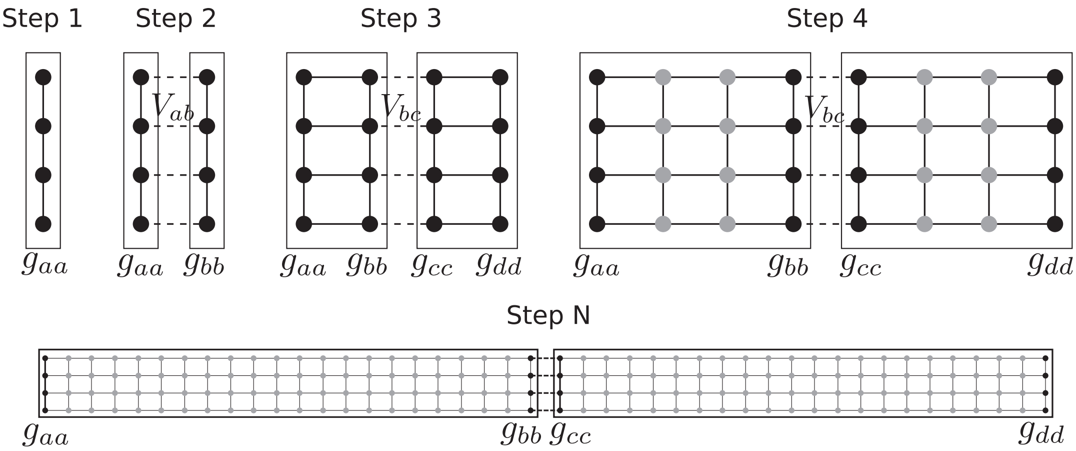
Step 1
Step 2
Step 3
Step 4
V_{ab}
V_{bc}
V_{bc}
g_{aa}
g_{aa} g_{bb}
g_{aa} g_{bb} g_{cc} g_{dd}
g_{aa} g_{bb} g_{cc} g_{dd}
Step N
g_{aa} g_{bb} g_{cc} g_{dd}

Figure B.1: Section-doubling algorithm for the calculation of surface Green's functions

$$G_{ba} = g_{bb} V_{ba} G_{aa}. \tag{B.4}$$

Step 3. Section doubling. Set $g_{aa} = G_{aa}$, $g_{bb} = G_{bb}$, $g_{ab} = G_{ab}$ and $g_{ba} = G_{ba}$. Add another copy of the two slices, $g_{cc} = g_{aa}$, $g_{dd} = g_{bb}$, $g_{cd} = g_{ab}$ and $g_{dc} = g_{ba}$. Calculate

$$G_{ba} = (1 - g_{bb} V_{bc} g_{cc} V_{cb})^{-1} g_{ba}, \tag{B.5}$$

$$G_{cd} = (1 - g_{cc} V_{cb} g_{bb} V_{bc})^{-1} g_{cd}, \tag{B.6}$$

$$G_{bd} = g_{bb} V_{bc} G_{cd}, \tag{B.7}$$

$$G_{ca} = g_{cc} V_{cb} G_{ba}, \tag{B.8}$$

$$G_{ad} = g_{ab} V_{bc} G_{ca}, \tag{B.9}$$

$$G_{da} = g_{dc} V_{cb} G_{ba}, \tag{B.10}$$

$$G_{aa} = g_{aa} + g_{ab} V_{bc} G_{ca}, \tag{B.11}$$

$$G_{dd} = g_{dd} + g_{dc} V_{cb} G_{bd}. \tag{B.12}$$

Step 4. Set $g_{aa} = G_{aa}$, $g_{ab} = G_{ad}$, $g_{ba} = G_{da}$ and $g_{bb} = G_{dd}$. Go back and repeat Step 3.

Step 5. When convergence is reached (that is, when G_{aa} and G_{dd} does not change), we have the lead surface Green's functions.

The functions G_{aa} and G_{dd} are our surface Green's functions, on the left and right side of the lead respectively. These can be directly used in the knitting-algorithm. To calculate the Γ-matrices at the surface atoms, we use the equation

$$\Gamma_a = i\left[\Sigma_a - \Sigma_a^\dagger\right], \tag{B.13}$$

where the self-energy matrices Σ are given by

$$\Sigma_a = V_{aa'}G_{a'a'}V_{a'a}. \tag{B.14}$$

Here, a' corresponds to the *single* slice next to a. To find $G_{a'a'}$, we simply just add a single slice at both ends of our infinite ribbon, and change indices so that the new slice gets index a, and the one that previously were a now is a'.

Bibliography

[1] B. C. Brodie, Philosophical Transactions of the Royal Society of London **149**, pp. 249 (1859).

[2] V. Kohlschütter and P. Haenni, Zeitschrift für anorganische und allgemeine Chemie **105**, 121 (1919).

[3] J. D. Bernal, Proceedings of the Royal Society of London. Series A, Containing Papers of a Mathematical and Physical Character **106**, pp. 749 (1924).

[4] O. Hassel and H. Mark, Zeitschrift für Physik **25**, 317 (1924).

[5] H. P. Boehm, R. Setton, and E. Stumpp, Pure and Applied Chemistry **66**, 1893 (1994).

[6] H. P. Boehm, A. Clauss, G. O. Fischer, and U. Hofmann, Zeitschrift für anorganische und allgemeine Chemie **316**, 119 (1962).

[7] P. R. Wallace, Phys. Rev. **71**, 622 (1947).

[8] G. W. Semenoff, Phys. Rev. Lett. **53**, 2449 (1984).

[9] D. P. DiVincenzo and E. J. Mele, Phys. Rev. B **29**, 1685 (1984).

[10] X. Lu, M. Yu, H. Huang, and R. S. Ruoff, Nanotechnology **10**, 269 (1999).

[11] A. K. Geim and K. S. Novoselov, Nature Materials **6**, 183 (2007).

[12] A. K. Geim *et al.*, Nature Materials **2**, 461 (2003).

[13] M. V. Berry and A. K. Geim, European Journal of Physics **18**, 307 (1997).

[14] K. S. Novoselov *et al.*, Science **306**, 666 (2004).

[15] K. S. Novoselov *et al.*, Nature **438**, 197 (2005).

[16] A. K. Geim, Angewandte Chemie International Edition **50**, 6966 (2011).

[17] K. S. Novoselov, Angewandte Chemie International Edition **50**, 6986 (2011).

[18] V. P. Gusynin and S. G. Sharapov, Phys. Rev. Lett. **95**, 146801 (2005).

[19] Y. Zhang, Y.-W. Tan, H. L. Stormer, and P. Kim, Nature **438**, 201 (2005).

[20] C. Berger *et al.*, The Journal of Physical Chemistry B **108**, 19912 (2004).

[21] F. Bonaccorso *et al.*, Materials Today **15**, 564 (2012).

[22] S. Park and R. S. Ruoff, Nature Nanotechnology **4**, 217 (2009).

[23] X. Huang *et al.*, Small **7**, 1876 (2011).

[24] O. C. Compton and S. T. Nguyen, Small **6**, 711 (2010).

[25] C. Lee, X. Wei, J. W. Kysar, and J. Hone, Science **321**, 385 (2008).

[26] A. A. Balandin, Nature Materials **10**, 569 (2011).

[27] F. Schwierz, Nature Nanotechnology **5**, 487 (2010).

[28] F. Bonaccorso, Z. Sun, T. Hasan, and A. Ferrari, Nature Photonics **4**, 611 (2010).

[29] D. A. Brownson, D. K. Kampouris, and C. E. Banks, Journal of Power Sources **196**, 4873 (2011).

[30] Y. Sun, Q. Wu, and G. Shi, Energy Environ. Sci. **4**, 1113 (2011).

[31] M. Pumera, Energy Environ. Sci. **4**, 668 (2011).

[32] M. Pumera, Materials Today **14**, 308 (2011).

[33] K. R. Ratinac, W. Yang, S. P. Ringer, and F. Braet, Environmental Science & Technology **44**, 1167 (2010).

[34] O. Klein, Zeitschrift für Physik **53**, 157 (1929).

[35] M. I. Katsnelson, K. S. Novoselov, and A. K. Geim, Nature Physics **2**, 620 (2006).

[36] N. Dombey and A. Calogeracos, Physics Reports **315**, 41 (1999).

[37] A. F. Young and P. Kim, Nature Physics **5**, 222 (2009).

[38] V. V. Cheianov, V. Fal'ko, and B. Altshuler, Science **315**, 1252 (2007).

[39] C. Beenakker, Phys. Rev. Lett. **97**, 067007 (2006).

[40] A. Tzalenchuk *et al.*, Nature Nanotechnology **5**, 186 (2010).

[41] A. H. Castro Neto *et al.*, Rev. Mod. Phys. **81**, 109 (2009).

[42] D. Abergel *et al.*, Advances in Physics **59**, 261 (2010).

[43] P. Avouris, Nano Letters **10**, 4285 (2010).

[44] S. Das Sarma, S. Adam, E. H. Hwang, and E. Rossi, Rev. Mod. Phys. **83**, 407 (2011).

[45] A. F. Young and P. Kim, Annual Review of Condensed Matter Physics **2**, 101 (2011).

[46] A. K. Geim, Science **324**, 1530 (2009).

[47] Y. Zhu *et al.*, Advanced Materials **22**, 3906 (2010).

[48] D. R. Dreyer, R. S. Ruoff, and C. W. Bielawski, Angewandte Chemie International Edition **49**, 9336 (2010).

[49] E. Y. Andrei, G. Li, and X. Du, Reports on Progress in Physics **75**, 056501 (2012).

[50] L. E. Foa Torres, S. Roche, and J.-C. Charlier, *Introduction to Graphene-Based Nanomaterials: From Electronic Structure to Quantum Transport* (Cambridge University Press, Cambridge, 2014).

[51] C.-H. Park and N. Marzari, Phys. Rev. B **84**, 205440 (2011).

[52] P. L. McEuen *et al.*, Phys. Rev. Lett. **83**, 5098 (1999).

[53] C. L. Kane and E. J. Mele, Phys. Rev. Lett. **78**, 1932 (1997).

[54] A. Cresti, R. Farchioni, G. Grosso, and G. P. Parravicini, Phys. Rev. B **68**, 075306 (2003).

[55] A. Cresti, G. Grosso, and G. P. Parravicini, The European Physical Journal B-Condensed Matter and Complex Systems **53**, 537 (2006).

[56] A. Cresti, Journal of applied physics **100**, 053711 (2006).

[57] G. Metalidis and P. Bruno, Phys. Rev. B **72**, 235304 (2005).

[58] C. H. Lewenkopf and E. R. Mucciolo, Journal of Computational Electronics **12**, 203 (2013).

[59] G. Thorgilsson, G. Viktorsson, and S. Erlingsson, Journal of Computational Physics **261**, 256 (2014).

[60] K. Kazymyrenko and X. Waintal, Phys. Rev. B **77**, 115119 (2008).

[61] C. W. Groth, M. Wimmer, A. R. Akhmerov, and X. Waintal, New Journal of Physics **16**, 063065 (2014).

[62] Intel, Math Kernel Library, http://software.intel.com/intel-mkl.

[63] OpenMP, The OpenMP API specification for parallel programming, http://www.openmp.org.

[64] L. Dagum and R. Menon, Computational Science Engineering, IEEE **5**, 46 (1998).

[65] M. B. Kennel, arXiv preprint physics/0408067 (2004).

[66] L. Brey and H. A. Fertig, Phys. Rev. B **73**, 235411 (2006).

[67] K. Nakada, M. Fujita, G. Dresselhaus, and M. S. Dresselhaus, Phys. Rev. B **54**, 17954 (1996).

[68] L. Brey and H. A. Fertig, Phys. Rev. B **73**, 195408 (2006).

[69] K. Wakabayashi, K. ichi Sasaki, T. Nakanishi, and T. Enoki, Science and Technology of Advanced Materials **11**, 054504 (2010).

[70] J. M. Carlsson, L. M. Ghiringhelli, and A. Fasolino, Phys. Rev. B **84**, 165423 (2011).

[71] A. S. Inc., Materials Studio release 7.0, 2013.

[72] B. I. Halperin, Phys. Rev. B **25**, 2185 (1982).

[73] M. Büttiker, Phys. Rev. B **38**, 9375 (1988).

[74] T. J. B. M. Janssen *et al.*, Reports on Progress in Physics **76**, 104501 (2013).

[75] C. Chua *et al.*, Nano Letters **14**, 3369 (2014).

[76] T. Yager *et al.*, Nano Letters **13**, 4217 (2013).

[77] Y. Nam *et al.*, Applied Physics Letters **103**, 233110 (2013).

[78] E. N. Economou, *Green's Functions in Quantum Physics* (Springer, New York, 2006), Vol. 7.

[79] S. Datta, *Electronic transport in mesoscopic systems* (Cambridge university press, Cambridge, 1997).